Additive Manufacturing, Volume 48, Part A, December 2021, Article number 102379
DOI:10.1016/j.addma.2021.102379

Scalable Wear Resistant 3D Printed Slippery Liquid Infused Porous Surfaces (SLIPS)

Hamza Shams[1,2], Kanza Basit[2], Muhammad Ali Khan[1], Asif Mansoor[2], Sajid Saleem[2]

[1]*Cranfield University, United Kingdom*
[2]*National University of Sciences and Technology (NUST), Pakistan*

Abstract

Surface wettability is a measure of adhesion and repulsion of liquids on a material's surface, where surface wettability may be altered by creating a new interfacial surface between the base material and the target liquid on top. Where the interface comprises of a liquid that is locked in the pores or ridges of the base material, it is then termed as liquid infused surface (LIS). LIS alters the wettability due to the distinctive properties of the interfacial liquid which now forms the new surface. If the interfacial liquid is repellent towards polar (hydrophobic) and non-polar (oleophobic) liquids, the overall surface becomes slippery (amphiphobic) and prevents any new target liquids from adhering. This phenomenon leads to the definition of slippery liquid infused porous surfaces (SLIPS), where this term not only describes its role but also its fabrication route.

Here a two-step facile method is presented to quickly transform any 3D printable polymeric material into robust SLIPS, irrespective of the wettability properties of the original polymer. The complex geometrical porosity required for locking the interfacial liquid is achieved using Fused Deposition Modelling (FDM) setup. Surface wettability characteristics of the 3D printed porous structure are then enhanced by increasing the liquid-adsorption sites where the locking of the infused interfacial (repellent) liquid takes place. The SLIPS demonstrate low rolling-off (sliding) angles with both polar and non-polar solvents of up to 2 degrees with high resistance to mechanical abrasion undergoing sliding frictional wear. The robust SLIPS as produced can be quickly scaled up using existing processes used in the laboratory.

Keywords: *SLIPS, Reentrant Geometry, Fused Deposition Modelling, Surface Wettability, Wear Resistance.*

Introduction

The term Slippery Liquid Infused Porous Surfaces (SLIPS) refers to modification of surface wettability characteristics by entrapment of a highly repellent liquid inside a porous solid mesh [1]. The phenomenon is originally seen on the leaves of *Nepenthes* Pitcher plant, which can alter their natural wettability state to either repel a multitude of liquids and solids from its surfaces or attract insects to entrap them as prey [2,3].

SLIPS are characterized as a porous surface, with a repellent fluid locked in micropores (solid) or impregnated in a gel such that this fluid adsorbs (wets) over the substrate completely but repels and is completely immiscible with the target fluid on top of it [4,5]. The idea of SLIPS was first coined in 2011 by Wong et al. which was based on the study of chemically etched Teflon mats that were impregnated with fluorinated oil [1]. From there on, SLIPS have been created using various methods, including the use of nanofiber mats [6–8], lithographic structures [5,9–13]. electrodeposition [14,15], coarsening of surfaces [16–18], embedding nanoparticles [19–21], porous membranes [22,23], and colloid layouts [24]. Previously,

Published by Elsevier. This is the Author Accepted Manuscript issued with: Creative Commons Attribution Non-Commercial No Derivatives License (CC:BY:NC:ND 4.0).
The final published version (version of record) is available online at DOI:10.1016/j.addma.2021.102379. Please refer to any applicable publisher terms of use.

fabricated SLIPS were generally limited to flat plane surfaces and single-sided substrates, however, the work of Geraldi et al. demonstrated the use of double-sided SLIPS with extremely low water contact and sliding angles [25]. Similarly, SLIPS with vertical flat-plate [26] and tubular [27–29] substrates have also been successfully fabricated with conforming results.

The major aim behind these surface preparations is to create a surface with such wetting properties that enables stabilization of infused or entrapped liquid when a target droplet is present, thus, lowering the overall surface energy which allows for easy roll-off (low sliding angles) of the target droplet. The stability of SLIPS can be determined by calculating the coefficient of spreading of the entrapped liquid (oil) which is given by Equation 1,

$$S_{ol} = \gamma_l - (\gamma_o - \gamma_{ol}) \quad (1)$$

where, S_{ol} is the coefficient of oil spreading, γ_l is the vapour tension of the target liquid, γ_o is the vapour tension of entrapped liquid and γ_{ol} is the interfacial tension between entrapped and target liquid. In ideal SLIPS, cloaking (wrapping up of entrapped liquid on target liquid) does not occur and the two liquids remain detached from each other that is $S_{ol} < 0$.

SLIPS find their commercial utility in fabrication of highly structured liquid repellent surfaces which may be hydrophobic (water repellent), oleophobic (oil repellent) or a combination of both, i.e. amphiphobic [30] depending on the properties of the entrapped liquid [31].

Previously, fabrication of the porous surface required high-end processes like Photolithography [11], Photopolymerization [32] and Laser Irradiation [33], due to the requirement of obtaining complex surface morphology for liquid entrapment. But recently, many low-cost, scalable, and simple methods to produce SLIPS have been identified by researchers [27–29,34]. The surface morphology plays a key role in not only supporting the infused liquid but more importantly providing strength against wear and tear so that the surface's performance remains intact over time.

The fabrication of the complex surface morphology has remained a big challenge till now because of the cost of processing such a fine resolution micro- and nano- porous surface. To address this, various high resolution 3D printing techniques have been used in recent years which tend to offer high level of control on final form [35,36]. Thereafter, liquid entrapment is carried out directly or after further post-processing of the printed surface.

In a move to explore the potential of low-resolution 3D printing techniques, we demonstrated earlier how processes like Fused Deposition Modelling (FDM) can be suitably used to alter surface wettability characteristics without the need of a post-fabrication treatment [37]. This is possible due to the unique ladder (staircase) geometry formed due to layer-by-layer deposition of FDM process which results in a unique reentrant geometry where air-entrapment takes place between the layers [38]. However, further investigation revealed that with scaling up of our current design, air entrapment becomes more challenging due to geometrical errors. A need was therefore realized to change the surface design by making it more scalable where the design's performance may be increased by replacing the entrapped fluid (air) to a more stable substitute thereby transforming them into SLIPS.

Building on this, we now introduce a two-step facile method of quickly transforming a 3D printed surface created using FDM into robust SLIPS with high resistance to mechanical abrasion. The SLIPS as obtained can easily displace polar and non-polar solvents at sliding angles of up to 2 degrees owing to the specific properties of the entrapped liquid on the

substrate surface which to the best of our current knowledge is one of the lowest sliding angles reported till date as can be compared from Table 1. These unique surfaces have precise geometrical features which are easy to fabricate using standard desktop based FDM 3D printing equipment.

Table 1: Comparison with respect to different substrate-lubricant combinations in polymeric SLIPS resulting in lowest slip angle of water droplet

S/No.	Substrate	Lubricant	Slip Angle Recorded (°)	Reference
1	PolyHIPE	PDMS	3±1.3	[39]
2	PDMS–PtBA–PiBuPOSSMA triblock copolymer	PDMS	6	[40]
3	HE-co-EDMA-based PPM	Krytox 100	4 to 6	[41]
4	PDMS/PA mixture at ratio 1:1:20	Black Seed Oil	10	[42]
5	PTFE-PVDF composite membrane	a. PDMS b. Ethyl Oleate c. PFPE	a. 11 b. 8 c. 10	[43]
6	Layer-by-Layer assembly of polyethylenimine and Nafion	Krytox 100	< 5	[44]
7	Glaco® Mirror Coat on Glass Slide	Silicone Oil	< 1.5	[25]
8	PDMS-OCH_3 (Surface Liquid Layer)	-	5	[45]
9	ULDPE Film	Vegetable Oils	< 5	[46]

In the sections to follow, we have first discussed on how the surface design was iterated upon along with the associated shortcomings. The discussion then moves towards the wettability testing of our proposed design and how we were able to convert anisotropic surface wettability to isotropic surface wettability by fabrication of SLIPS. After characterizing surface wettability, we go one step further in estimating changes in surface free energy with subsequent surface treatment and discuss the wear failure criterion that can limit the functionality of SLIPS when exposed to harsh frictional wear.

Iterative Surface Design

The concept of using reentrant geometries for resisting penetration and adhesion of liquids on the surface without the need of a repellent coating is well-established [47–53]. However, fabrication of reentrant geometries pose a challenge in fabrication of complex geometry which facilitates formation of air entrapment sites especially with the use of 3D printing processes [37]. Moreover, until recently, FDM has not been reported as a favoured choice for creation of reentrant geometries due to the limitation in obtaining a reasonably small surface area for air entrapment [37,38].

In a first, our group demonstrated a preliminary experiment using the ladder effect formed due to layer-by-layer deposition in FDM for increasing the surface area to create these air entrapment sites as shown in Figure 1.

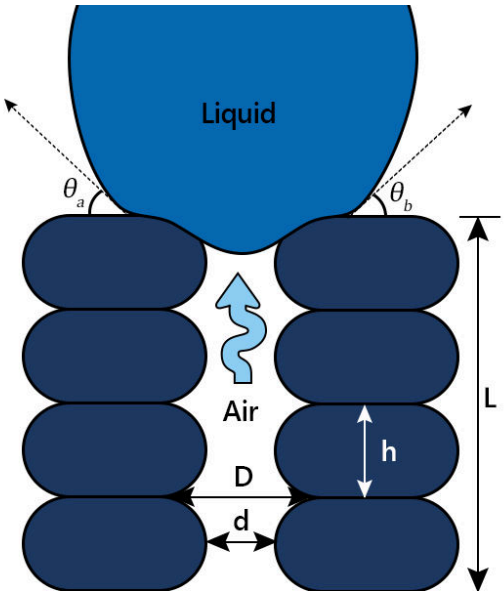

Figure 1 a) Illustration of air entrapment between two printed structures (θ_a is left contact angle, θ_b is right contact angle, D is groove spacing between two adjacent inside edges, d is groove spacing between two adjacent outside edges, h is the layer height and L is the length of overall printed structure) [38]

High contact angles with water (polar) and glycerol (non-polar) were favourably achieved and retained without any surface treatment. However, our subsequent experiments demonstrated that while it may be easier to maintain this in a laboratory environment, scaling up to speed up process times and increase overall surface size results in bigger gaps between individual reentrant geometries which are highly susceptible to liquid penetration.

To counteract this, a change in the design geometry was considered by using the widely reported sponge-design [54–56] which works on printing line layers in alternating parallel and perpendicular directions and print the final geometry using FDM. The line width was adjusted based on the nozzle orifice diameter and hollow sponge geometries were favourably fabricated as shown in Figure 2.

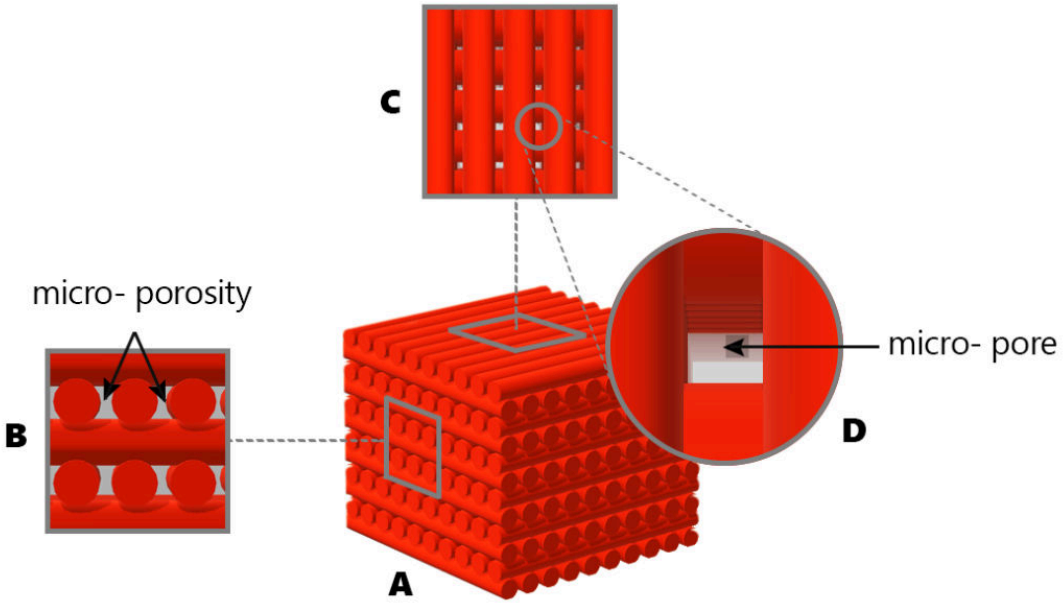

Figure 2: Modelled cubic sponge designed by overlapping of parallel and perpendicular line layers. The resultant model has micro porosity on all 6 sides of the cube. (a) Shows the isometric view of the cubic sponge model. (b) Shows the micro porosity from the side while (c) shows the micro porosity from the top. (d) Inset shows a close-up of the micro – pore whose design is based on the reentrant geometry ladder effect explained by Shams et al. [37]

The pore diameter (space between 2 parallel lines) was adjusted based on the minimal XY resolution (0.20 mm) of a desktop FDM printer as shown in Figure 3. However, the overall structure did not preserve any repellent behaviour and the target liquids easily flowed through.

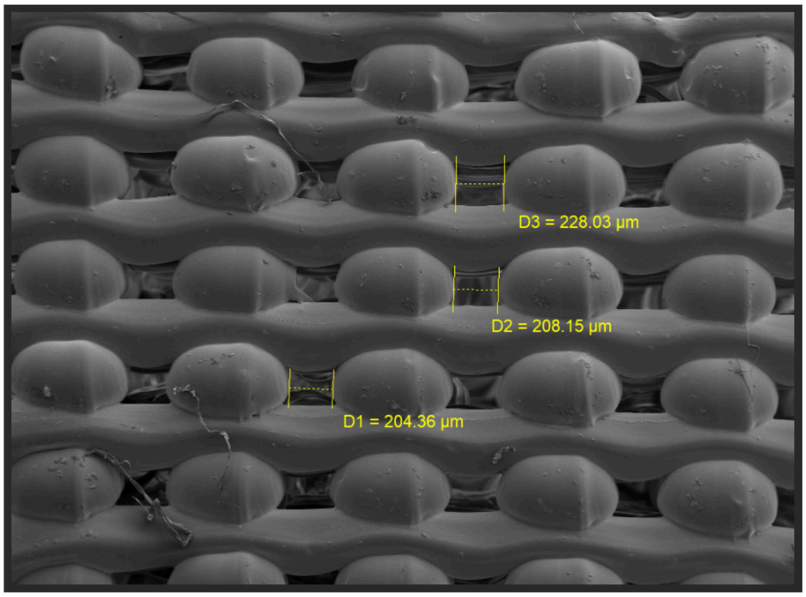

Figure 3: Scanning Electron Micrograph (side-view) of the Sponge profile where the micro-porosity is in the range of 0.20 mm (200 microns)

Further scaling down of geometry was not possible due to the limitation of slicing algorithms used by FDM printers which were unable to analyse such small features adequately and hence generated errors when trying to resolve distance between 2 parallel lines beyond a certain threshold value. The threshold value as observed was governed by the nozzle orifice diameter. This prevented us from setting the size of the pore near to or less than the nozzle orifice diameter without it becoming a single entity during slicing. However, this limitation no longer existed when the same printer was programmed to print infill patterns.

This inspired us to use this feature to our advantage by translating infill patterns on the substrate's surface using modifiers. This not only catered to the difficulty of designing complex CAD geometries for this purpose but in fact made the designing easy which now comprised only of simple Boolean operations followed by computations carried out by the slicing algorithm. The 3D lattice hence created provides 3-dimensional micro- porosity over the entire depth of the specimen with smooth reentrant edge geometry on the top.

Each line's width in the infill pattern is still controlled by the nozzle's orifice diameter but the spacing between the lines can now be easily adjusted by altering infill percentage. Where required, further tinkering was also possible by modifying the source code (available as open source) of the infill pattern or by choosing a new infill pattern altogether. This allowed us to reduce the porosity size considerably as shown in Figure 4.

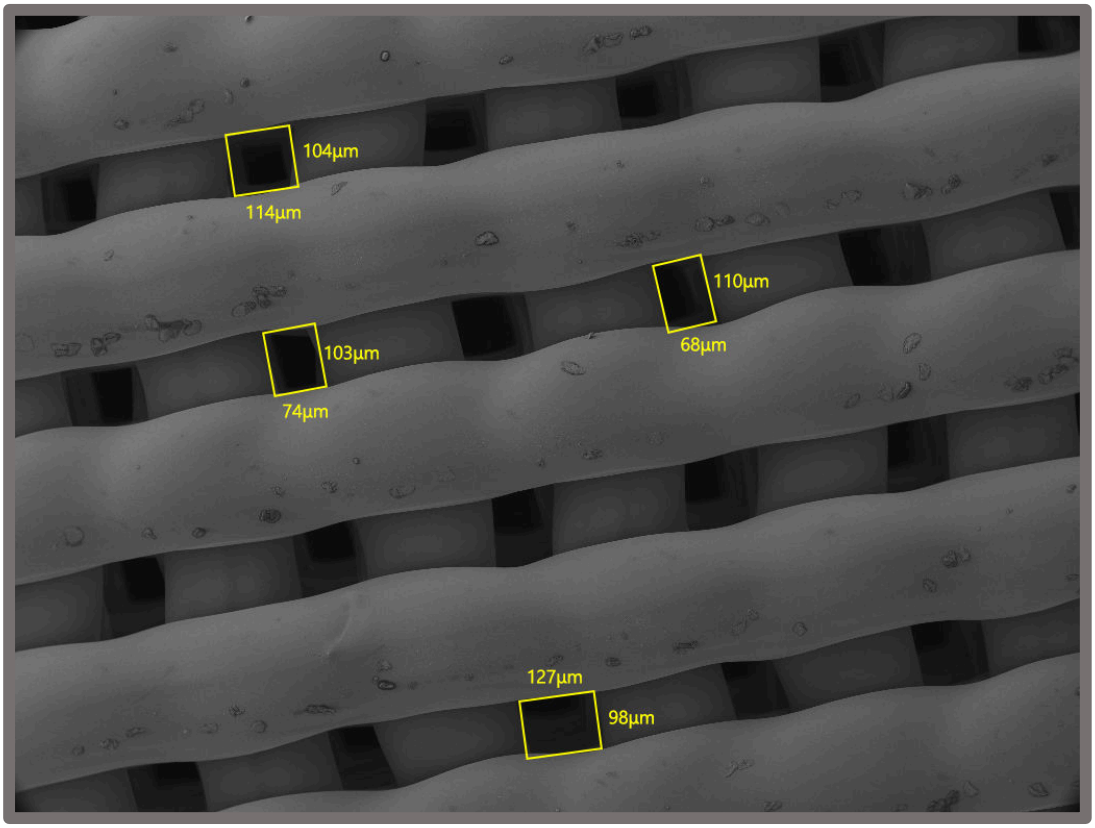

Figure 4: Scanning Electron Micrograph (top-view) of sponge profile created using 0.15 mm nozzle (150 microns) with suitable iteration of infill density to get very precise geometrical micro-pores.

Design of SLIPS

Preliminary Investigation

To demonstrate the utility and ease of creation of our newfound surfaces, we developed a test specimen using grid as the infill pattern and recorded contact angles and sliding angles in and against the printing direction. This 2-direction analysis is important because an FDM printer prints grid infill pattern as lines stacking up layer-by-layer, which means that the wettability properties differ in and against the printing direction due to formation of surface ravines between 2 parallel lines.

It was observed that the target liquids were not able to penetrate the structure despite wetting the top surface completely as shown in Figure 5. No formation of air bubbles or liquid seepage was visible even after the leaving the specimens in open air for an hour. A comparison image showing the same droplet at time 0 and time 60 mins is provided in Figure 1 of **Supplementary Information**. Till this point, no surface treatment was carried out on the 3D printed specimen and the surface repellence was attributed to the air entrapment within the reentrant geometry sites.

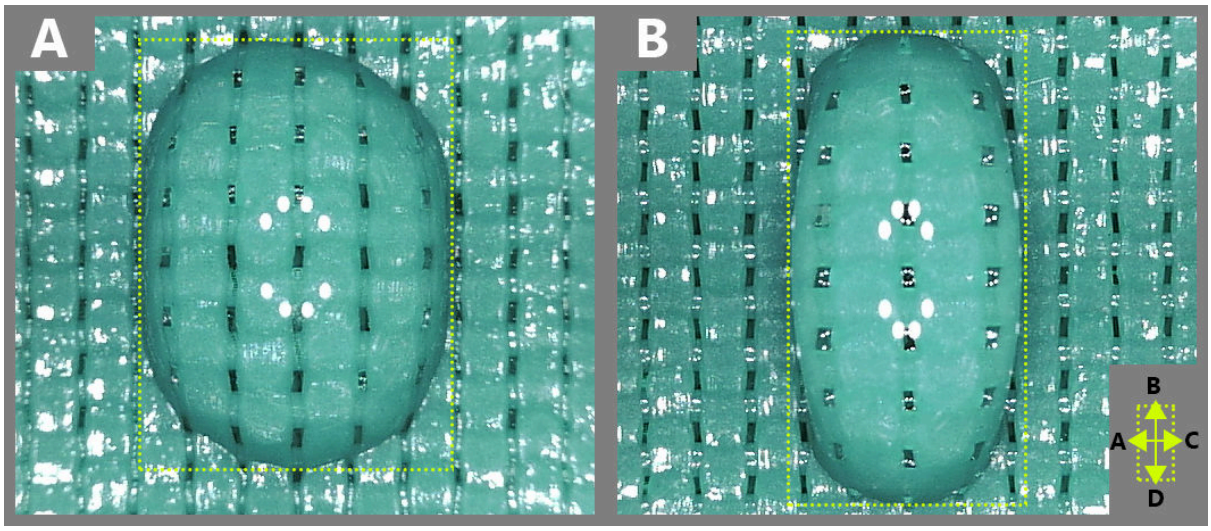

Figure 5: (a) 20µl double distilled water droplet (target liquid 1) resting on the top surface and (b) 20µl glycerol droplet (target liquid 2) resting on the top surface, without any penetration in the holes (reentrant profiles). The target liquids can easily flow in the printing direction (BD) while they face resistance in the other direction (AC) which leads to anisotropic wettability.

However, it was observed that the printing direction played a major role leading to anisotropic surface wettability where printed lines support the flow of target liquid parallel to them while act as anchoring (ravines) sites when the target liquid flows perpendicularly. This makes it suitable for use in environments where directional flow is considered imperative but limit its utility as a widespread isotropically amphiphobic surface. This investigation is well in line with our previously reported work [37].

To make the surface demonstrate isotropic wettability, the surfaces were converted to SLIPS by replacing air with a repellent oil within the structure. The surfaces resulting directly from FDM have micro- porosity in the range of 150 – 250 µm (based on nozzle orifice diameter) and are extremely smooth (R_q RMS between 1 to 5µm) which is not suitable to be used directly as SLIPS which requires oil adsorption at nano- levels. An experimental scheme was therefore developed to increase the surface area or oil adsorption sites by altering the surface roughness directly or by adding oil adsorbing particles where oil may be trapped over which target liquids can easily roll off allowing the surface to exhibit isotropic wettability.

Experimental Methodology

Preparation of 3D Printed Specimens

Square discs measuring 20 mm x 20 mm x 2 mm were prepared using Prusa MINI 3D Printer which is a standard desktop kit printer from Prusa Research. Grid infill pattern available in Prusa Slicer were translated onto the face and depth of the specimen using modifiers during the slicing process with a marginal error of 3% between the sliced and the as-built part. Comparison of sliced and as-built part can be found in the **Supplementary Information**. 150 µm and 250 µm nozzle orifice diameters were used to print the samples. The printing parameters are provided in Table 2.

Table 2: 3D printing parameters for translation of infill geometry on the specimen.

Printing Parameter	Value
Material	colorFabb Mint Turqoise PLA Filament
Nozzle/Bed Temperature	210°C / 60°C
Printing Speed	15 mms^{-1}
Infill Pattern	Grid

Infill Density	99%
Nozzle Diameters	150 µm and 250 µm
Modifiers	Cylindrical
Top/Bottom Layers	0/1

The discs therefore had 5 nonporous shells (on the side) on 1 porous surface on the top where the infill is exposed which forms reentrant geometry as shown in Figure 6.

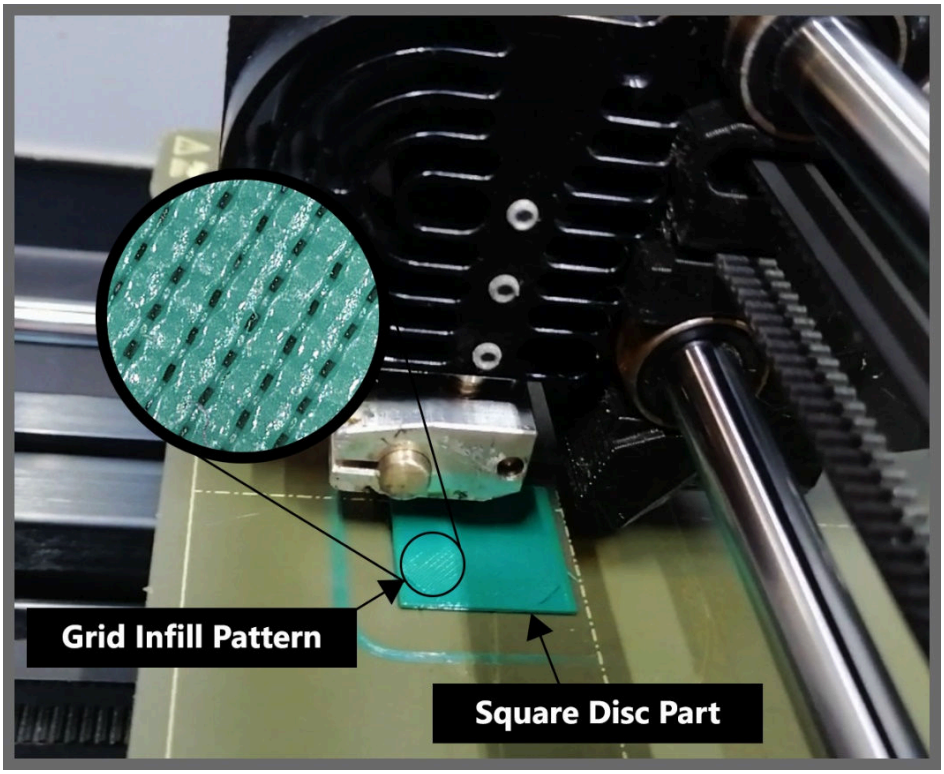

Figure 6: 3D printing of disc specimens where the inset shows the grid infill pattern being deposited in the centre of the square disc.

A top view of the sliced model along with actual part is shown in Figure 7 to compare how the grid infill pattern is translated into the actual part geometry. Furthermore, the AC-BD direction rectangle where AC relates to against the printing direction, while BD refers to in printing direction has been mapped on to the specimen which forms basis of our further investigation.

It may be noted that this apparent anisotropic wettability characteristic is not visible in the sliced model (on computer screen) where the infill pattern appears to be in a single plane. Furthermore, since the infill percentage is kept constant, samples prepared using 150 microns nozzle have more lines printed per unit area in order to cover the open spaces. This can be seen in scanning electron micrographs of control samples prepared using 150 microns nozzle as shown in Figure 3 of **Supplementary Information**.

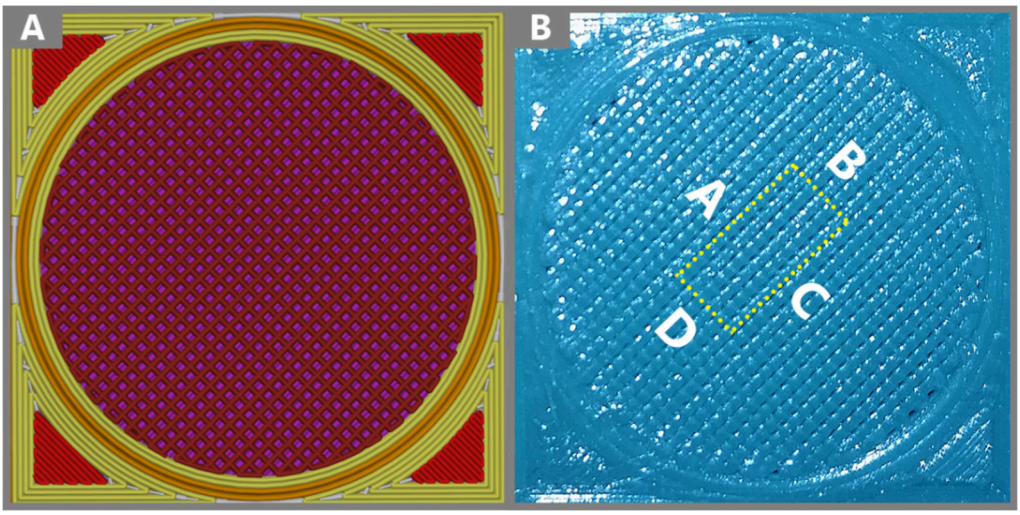

Figure 7: (a) The sliced model on computer screen and (b) actual printed part shown together to show how the grid infill pattern is translated. The AC-BD direction rectangle mentioned previously has also been mapped on the specimen to show the printing direction.

Surface Preparation

The printed substrate was then eroded to create micro- and nano-porosity on the top surface and on the depth (inside) of the specimen using solutions prepared by combination of 2-Butanone (commonly known as Methyl Ethyl Ketone (MEK)) obtained from Fisher Scientific UK and 2 variants of Cab O Sil® namely M5 and TS720 (amorphous fumed silica powder) obtained from INOXIA Ltd as shown in Table 3.

MEK and silica powder were mixed in weight proportion of 99% and 1% respectively. Samples were dipped in the solution and stirred vigorously at 1000 rpm using a magnetic stirrer for up to 5 mins to ensure erosion of the top 3D printed layer and complete penetration of the solution inside the discs to create homogenous micro- and nano- porosity. The penetration of the liquids can be visualized by the escaping air bubbles from the sample while stirring.

The eroded samples were then completely cleaned of residual solution by washing them with Isopropanol in magnetic stirrer which also helped in removal of any free debris. The samples where then left to dry overnight in open air.

Table 3: Types of treatments carried out to prepare samples for further investigation

Sample Type	Treatment	Remarks
A	Untreated	Control 1
B	Silicone Oil	-
C	Krytox GPL-105	-
D	MEK	Control 2
E	MEK + Silicone Oil	-
F	MEK + Krytox GPL-105	-
G	MEK + M5	Control 3
H	MEK + M5 + Silicone Oil	-
I	MEK + M5 + Krytox GPL-105	-
J	MEK + TS720	Control 4
K	MEK + TS720 + Silicone Oil	-
L	MEK + TS720 + Krytox GPL-105	-

All control samples were imaged using TESCAN S8000 scanning electron microscope to observe effects on surface changes and creation of micro- and nano- porosity. Figure 8 shows the scanning electron micrographs of the control samples prepared using 250 µm nozzle. The imaging of oil infused samples was difficult due to the gradual evaporation of oils in low vacuum pressure (0.002 Pa).

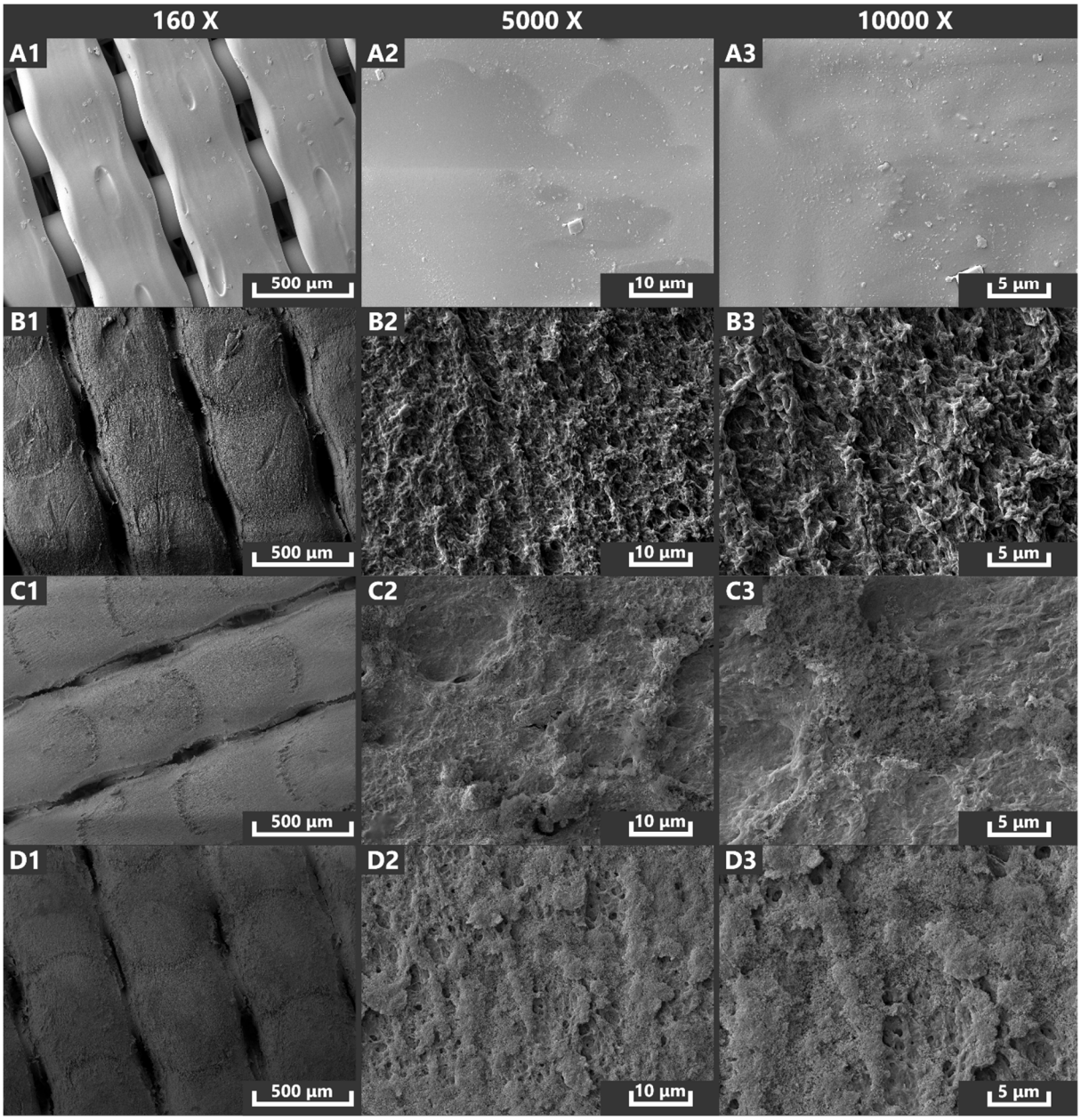

Figure 8: Scanning electron micrographs of control samples prepared using 250 µm nozzle before entrapment of liquid. The 1,2 and 3 suffixes after the letters denote the 160X, 5,000X and 10,000X magnifications respectively. The (a) shows Sample A (b) shows Sample D, (c) shows Sample G and (d) shows Sample J after undergoing control treatments.

A change in surface roughness due to creation of micro- and nano- porosity in Figure 8 B2 and B3 is evident. It can further be observed in Figure 8 C2 and D2 that the amorphous fumed silica powder settles in the holes created using MEK which gives the surface its own distinctive properties governed by the type of powder.

The samples were also analysed using Energy Dispersive Spectroscopy (EDS) to identify and characterize regions of silica deposition which were found to be clumped and randomly distributed along the printed layers. Figure 9 shows an EDS spectrum with an inset scanning electron micrograph of sample G printed using 250 microns nozzle.

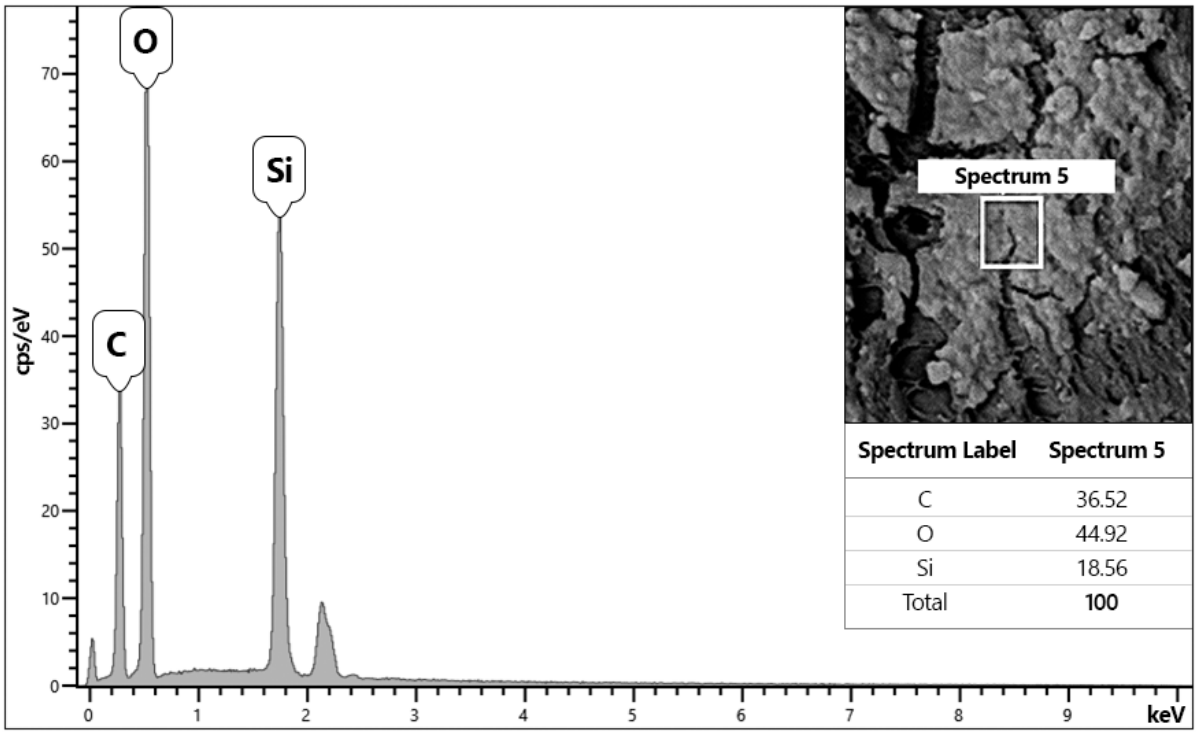

Figure 9: EDS performed on a randomly selected region in Sample G prepared using 250 µm nozzle before entrapment of liquid. Inset image shows the clumped deposition of silica powder. The table below the inset shows the percentage weight of each identified element during EDS.

Entrapment of Repellent Liquid

2 liquids, 350cst Silicone Oil and Krytox GPL-105 (perfluoropolyether (PFPE); a low surface tension oil insoluble in water) which are known for their repellent properties [57–60] were used as the entrapped liquids. Table 3 provides details of the complete set of experiments performed using the 2 liquids. For reliability, experiments were repeated where required and average of readings was recorded. Eroded-dried- samples were stirred in the liquid baths containing one of the repellent liquids for 5 minutes. Formation of air bubbles indicated the seeping in of the repellent liquids. The samples were then turned upside down so that the residue (free) liquid drips out and then left to dry overnight at room temperature.

Contact Angle (CA) and Slip Angle (SA) Measurements

Evaluation of contact angle (CA) and slip angle (SA) was carried out with Double Distilled Water (DDW) and 99% Glycerol sourced from Fischer Scientific UK Ltd. Ossila Contact Angle Meter with equipment's base software were used to record the CA and SA. The droplet volume was kept constant at 20 µl in line with ASTM D7334-08. For the measurement of CAs, since the repellent liquids are completely immiscible with the target liquids [61], effects like cloaking (where the low surface tension repellent liquid fully engulfs the target liquid) have not been considered due to little visual evidence of wetting ridges at the periphery of the target liquid droplet as shown in Figure 10. Furthermore, evaluation of the loss of lubricant over time due to shear induced drainage or evaporation which are two significant sources of lubricant depletion in case of immiscible/non-cloaking liquid combinations was not considered. This means that $CA \cong CA_{app}$, where CA_{app} is the apparent contact angle formed on the liquid-liquid interface as explained in detail in later section. Measurement of CAs was performed 3 to 5 times in each direction and average of these readings was recorded along with standard deviation (SD) as evidenced in the Tables 1 to 4 of **Supplementary Information**.

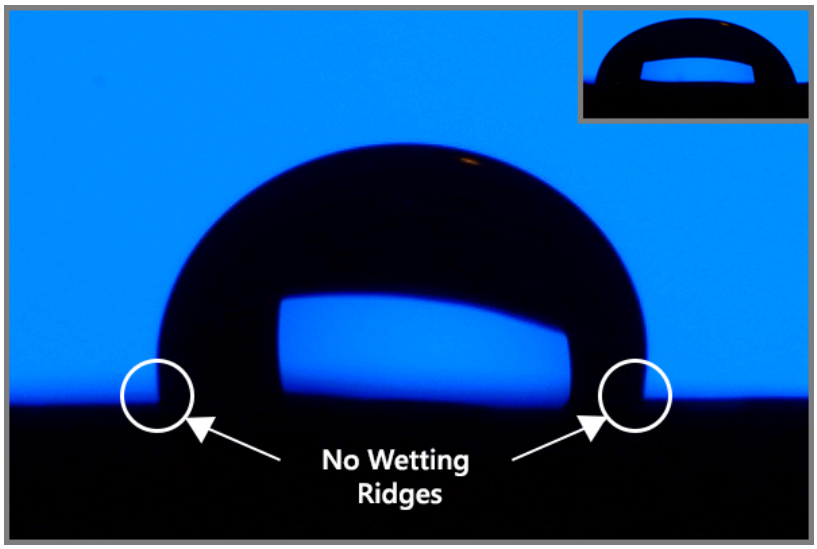

Figure 10: CA measurement screen of Sample K (250 microns) with water and glycerol (inset) in BD direction (spreading). The side wetting ridges which are characteristic of liquid-liquid interaction are not distinctively visible.

Recording of slip angle was performed by tilting the sample from 0 to 15 degrees using a calibrated goniometer stage sourced from Thorlabs. The choice of using this stage was based on recording low slip angles where pinning of the target liquid on the final interfacial surface does not occur. The slip angle was recorded when the droplets showed constant slipping in A to C and B to D directions (refer to Figure 5 for definition of directions). The droplet movement was also recorded using a portable hand-held microscope to facilitate visualization of the phenomenon as shown in Figure 11. Readings were repeated for consistency and average values were recorded in each case.

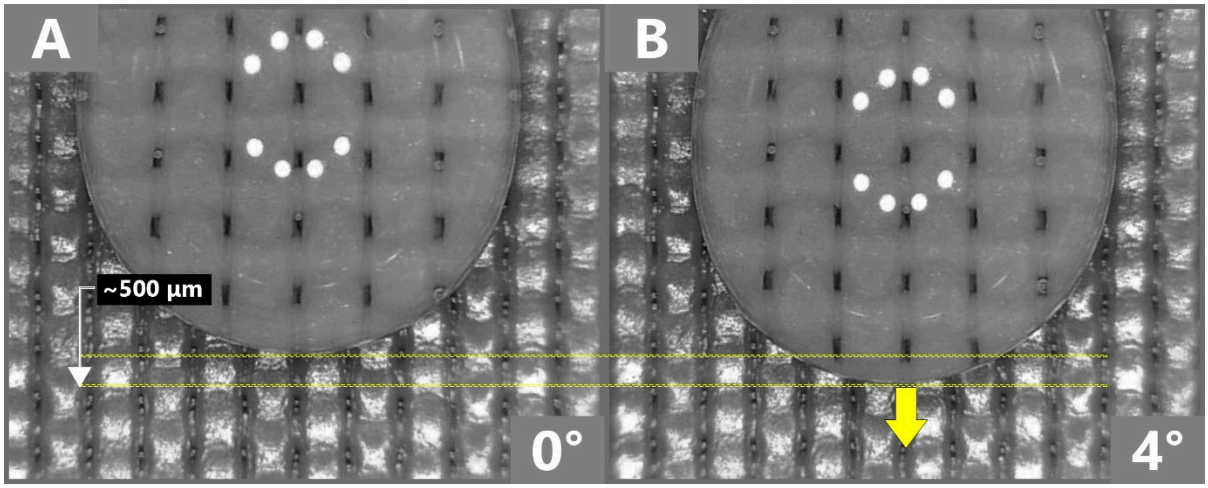

Figure 11: Recording of Slip Angles in BD direction of Sample K prepared using 250 microns nozzle. The sample rests on the goniometer stage and a portable microscope is used to record the continuous slipping of the target droplet on the surface as the stage tilt angle is increased in steps of degrees.

Testing for Wear Resistance

Surface robustness was evaluated using a TRB^3 Pin-on-Disk tribometer by Anton Paar as shown in Figure 12. The single pin-on-disk tribometer provides a constant normal load at a specific circumference of the specimen resulting in frictional wear. The instrument through its software provides various datasets including the pin's penetration depth with respect to cycles (time) and changes in coefficient of friction calculated as a function of normal and lateral forces on the pin. The characteristic pin (single-point load) can be replaced by a ball which spreads the normal force adequately on the specimen defined by the volume of the spherical cap which rubs with the specimen and is a function of the contacting surface area and the penetration

depth. Since in-situ volumetric wear profiles are hard to analyse, penetration depth gives a more simplistic approach to quantify linear wear.

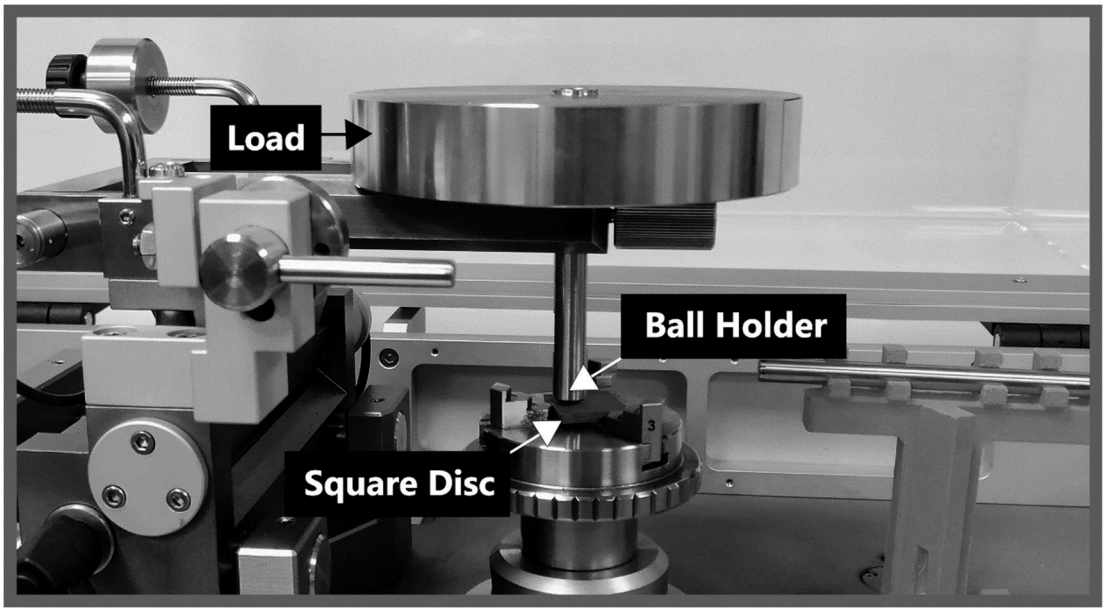

Figure 12: Tribometer setup for generating sliding wear on square disc samples.

The wear testing parameters are as given in Table 4. Surface robustness in relation to wear resistance and coefficient of friction changes was evaluated.

Table 4: Wear testing parameters

Testing Parameter	Value
Specimen Material	PLA
Ball Material	Al_2O_3
Ball Diameter	6 mm
Normal Force	20 N
Rotational Speed	200 RPM
Maximum Test Duration / Cycles	600s / 2000
Sliding Distance (From Centre)	5 mm

Results

Static CA and SA Measurements

The Static CA results with water as the target liquid on samples prepared using 150 µm and 250 µm nozzle sizes are summarized in Figure 13, where the reference tables are provided in the **Supplementary Information**. Taking in consideration the printing direction, it is important to record both Static CA and SA in 2 directions that is, AC and BD as shown in Figure 5.

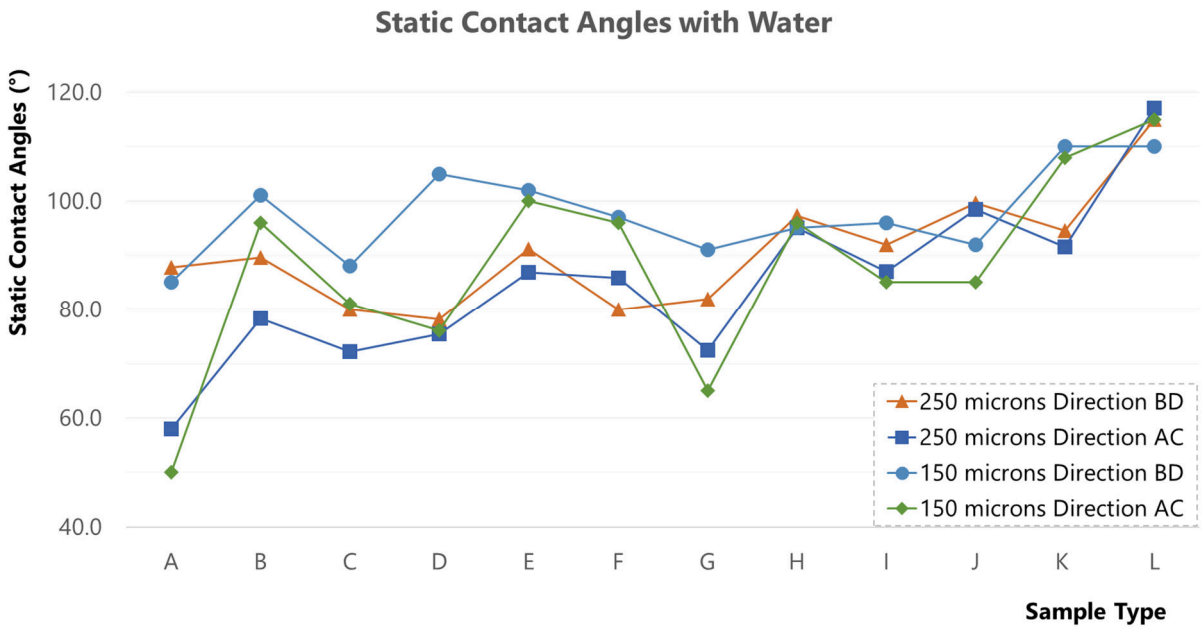

Figure 13: Summary of Static CA results with water as the target liquid on samples A - L prepared using 150 µm and 250 µm nozzle sizes.

A summary of SA with water for samples A – L is provided in Table 5.

Table 5: Summary of sliding angles of samples A - L with water as the target liquid

Sample Type	Sliding Angle (°) with Water			
	150 microns		250 microns	
	Direction BD	Direction AC	Direction BD	Direction AC
A	14.0	*	6.0	*
B	14.0	*	10.0	15.0
C	*	*	*	*
D	*	*	5.0	15.0
E	6.0	7.0	5.0	7.0
F	*	*	*	*
G	*	*	14.0	*
H	6.0	5.0	12.0	15.0
I	*	*	*	*
J	*	*	*	*
K	2.0	2.0	5.0	4.0
L	4.0	5.0	3.0	5.0

(*) indicates SA greater than 15 degrees.

Similarly, a summary of CA and SA with glycerol as the target liquid is provided in Figure 14 and Table 6 respectively.

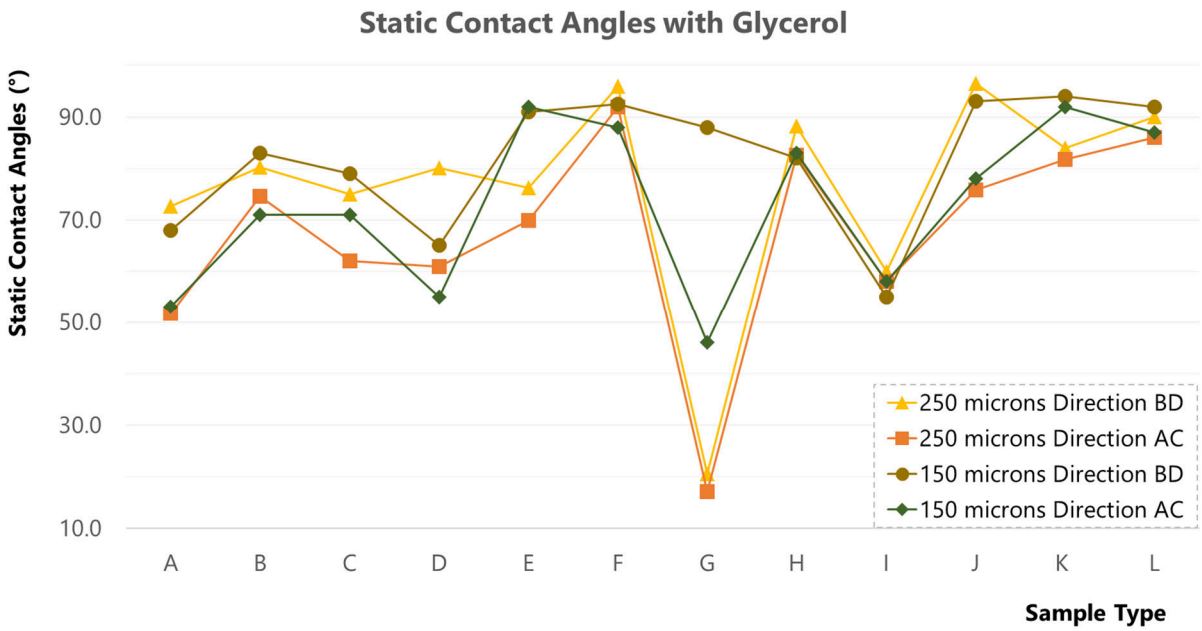

Figure 14: Summary of CA results with glycerol as the target liquid on samples A - L prepared using 150 µm and 250 µm nozzle sizes.

Table 6: Summary of sliding angles of samples A - L with glycerol as the target liquid

Sample Type	Sliding Angle (°) with Glycerol			
	150 microns		250 microns	
	Direction BD	Direction AC	Direction BD	Direction AC
A	5.0	*	2.0	*
B	4.0	5.0	2.0	5.0
C	*	*	*	*
D	*	*	3.0	*
E	3.0	4.0	7.0	9.0
F	12.0	15.0	10.0	13.0
G	*	*	2.0	8.0
H	4.0	4.5	5.0	14.0
I	*	*	*	*
J	*	*	9.0	6.0
K	2.0	3.0	2.0	3.0
L	3.0	4.0	3.0	4.0

(*) indicates SA greater than 15 degrees.

Surface Wettability

The CA results for water and glycerol clearly show the surface anisotropic wettability transitioning to isotropic wettability with the addition of repellent lubricants and conversion to SLIPS, where both CA in both AC and BD directions are getting closer to each other.

The most favourable surface treatment combination that results in ideal SLIPS characteristics is obtained in sample L, where the sample is first treated with hydrophobic fumed silica powder (TS720) and then impregnated with Krytox GPL-105 as the repellent oil. Sample L shows extreme resistance to surface wetting which can be seen from a high contact angle and low slip angles for both water and glycerol. This is attributed to the hydrophobic characteristics of the silica powder which are further enhanced with the addition of repellent oil. Similar behaviour is observed in sample K, where Krytox GPL-105 is replaced with silicone oil. While

sample K demonstrate limited anisotropic wettability by differing CAs in AC and BD direction, the sliding angles in either direction are very close to each other. This combination of TS720 and silicone oil in sample K, makes the 2 liquid droplets flow easily due to higher repellence as compared to other samples.

Conversely, the least favourable surface treatment was on sample G, a combination of MEK and amorphous fumed silica powder variant M5 which instead of repelling makes the surface more wetting or hydrophilic. This is attributed to the high adsorption capacity of the M5 silica powder for both polar and non-polar liquids. By exposing this surface to repellent oils as in the case of samples H and I, the adsorption capacity of the M5 powder becomes full and the target liquid no longer wets the surface as before.

Another important result is obtained in the case of sample E, where direct impregnation of silicone oil on MEK eroded surface also gives comparable results with sample K. Furthermore, while investigating samples prepared using 150-microns nozzle, the closer packing of the lines (as compared to samples prepared using 250 microns nozzles) facilitates the adsorption of silicone oil. This can be seen by overall higher CA and low SA obtained in samples B, E, H and K. The same however, is not observed in samples where Krytox GPL-105 is used as the repellent liquid.

Characterization of Wear Behaviour

It may be noted that the surface treatments (samples A – L) are not meant to strengthen the material. The actual strength of the material comes from the 3D printed structures, therefore wear measurement was carried out without any surface treatment to characterize the true wear behaviour of the reentrant geometries as shown in Figure 15.

Trendlines with cubic polynomial fitting were used to identify the relationship between coefficient of friction (COF) and penetration depth (Pd) over a fixed time and cycles setting as mentioned in Table 4.

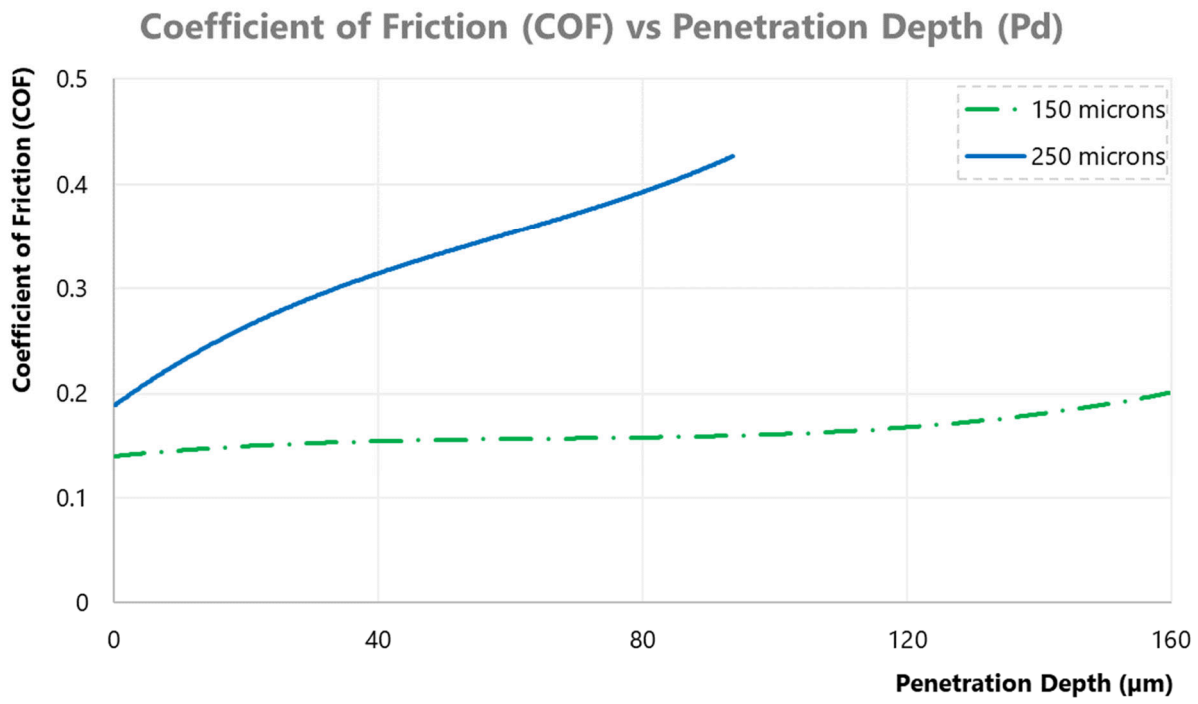

Figure 15: Relationship between coefficient of friction and penetration depth for the untreated samples created using 150- and 250-microns nozzles.

It can be observed that samples prepared using 250 microns nozzle show better resistance to wear which is indicated by a higher COF and lower Pd over the investigated time. However, the samples prepared using 150 microns nozzles are more susceptible to wear which is indicated by lower COF values and higher Pd over the investigated time. This is attributed to the small width of the printed layers in 150 microns (as compared to 250 microns samples) which easily give way under high sliding load conditions.

However, on an overall scale the penetration depth even after 2000 cycles is hardly 90+ microns in 250 microns samples and up to 160 microns in 150 microns samples which is indicative of high mechanical stability of our 3D printed surfaces.

This is important because surface deterioration by friction is a common phenomenon which can be modelled using a tribometer capable of generating continuous sliding wear. The long-term effects of sliding wear include reduction in the efficiency of surface repellence which is why it is important to identify failure criterion associated with our SLIPS geometry and this is discussed in detail later on.

Further Discussion

Estimation of Changes in Surface Free Energy (SFE)

The estimation of surface free energy (SFE) (interfacial energy in liquids) in SLIPS is not straightforward, due to liquid-liquid interface where distortions take place close to the surface caused by formation of a wetting ridge or effects of cloaking [62] when the two liquids interact as shown in Figure 16.

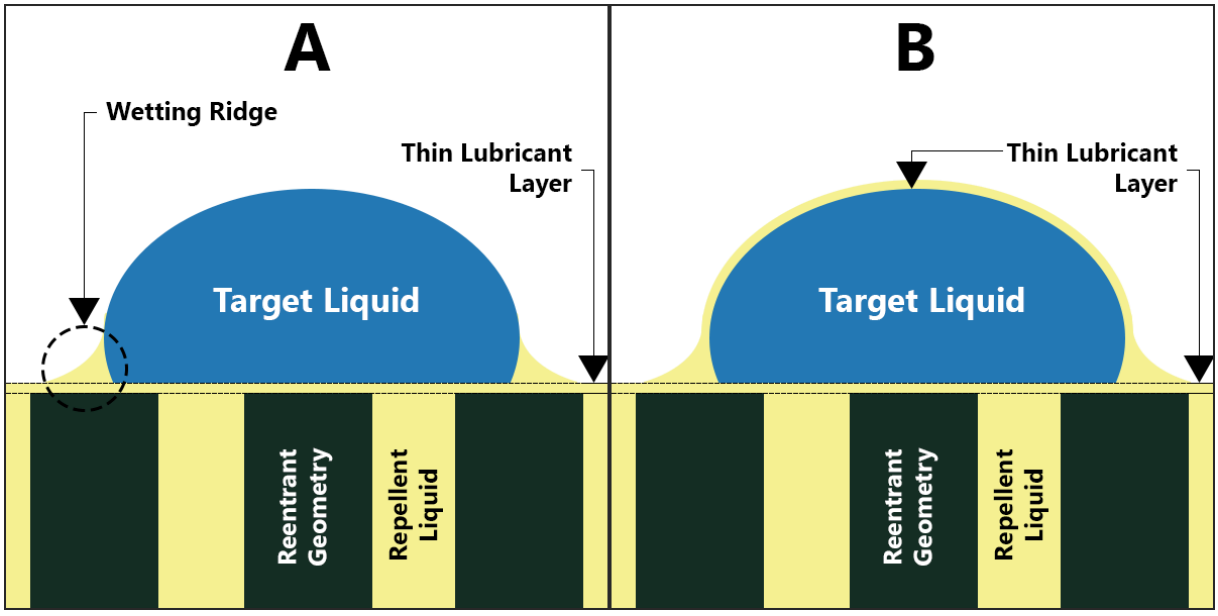

Figure 16: (a) Shows wetting ridge formed at the interface of target and repellent liquids while (b) shows cloaking effect where a thin lubricant layer covers the target liquid, both of which affect measurement of actual CA.

This leads to the formation of an apparent CA [63,64] instead of the Young's CA, where the CA model now takes the form of Equation 2.

$$\cos\theta_{app} = \frac{\gamma_{RV} - \gamma_{RT}}{\gamma_{TV}} \tag{2}$$

where θ_{app} is the apparent contact angle similar to Young's CA, γ_{RV} is the surface tension of the repellent liquid in vapour (air), γ_{TV} is the surface tension of the target liquid in vapour (air),

and γ_{RT} is the interfacial tension between repellent and target liquids. However, this is only true when the interaction is perfectly liquid-liquid.

In our case, the size of our reentrant geometry indicates that unless the liquid fully bathes the surface, the repellent liquid always forms an emergent profile as explained by Smith et al. [5], where surface profile plays a major role in stabilizing the repellent liquid by interlocking it in the micro- pores between the reentrant layers. This means that a fine layer of repellent liquid is formed on the reentrants' surface while the micro- pores are fully filled with repellent liquid. Therefore, the surface wettability effects are also influenced by surface geometry in SLIPS state as has been observed in previous section.

We therefore assume that in static conditions, the target liquid droplet is extremely close to the solid surface with an extremely thin repellent liquid layer in between having small translational perturbations such that the repellent liquid only brings changes in surface roughness as in the case of a regular coating. The polar and dispersive components of this newfound surface is treated in unison, that is a combination of liquid and solid surface instead of two separate entities.

By doing so, one can use the widely used Owen, Wendt, Rabel and Kaelble (OWRK) model [65] to estimate changes in surface energy while transitioning from sample A to sample L using water and glycerol as the reference liquids. The OWRK model can be expressed by the Equations 3 and 4.

$$\gamma_W(1+\cos\theta_W) = 2\sqrt{\gamma_{Sp}\gamma_{Wp}} + 2\sqrt{\gamma_{Sd}\gamma_{Wd}} \tag{3}$$

$$\gamma_G(1+\cos\theta_G) = 2\sqrt{\gamma_{Sp}\gamma_{Gp}} + 2\sqrt{\gamma_{Sd}\gamma_{Gd}} \tag{4}$$

The polar and dispersive components of the two liquids are given in Table 5 of **Supplementary Information**. Corresponding CAs of the same direction (either AC or BD) for water and glycerol are then used to evaluate changes in SFE and then averaged out. Changes in SFE from samples A – L are as shown in Figure 17.

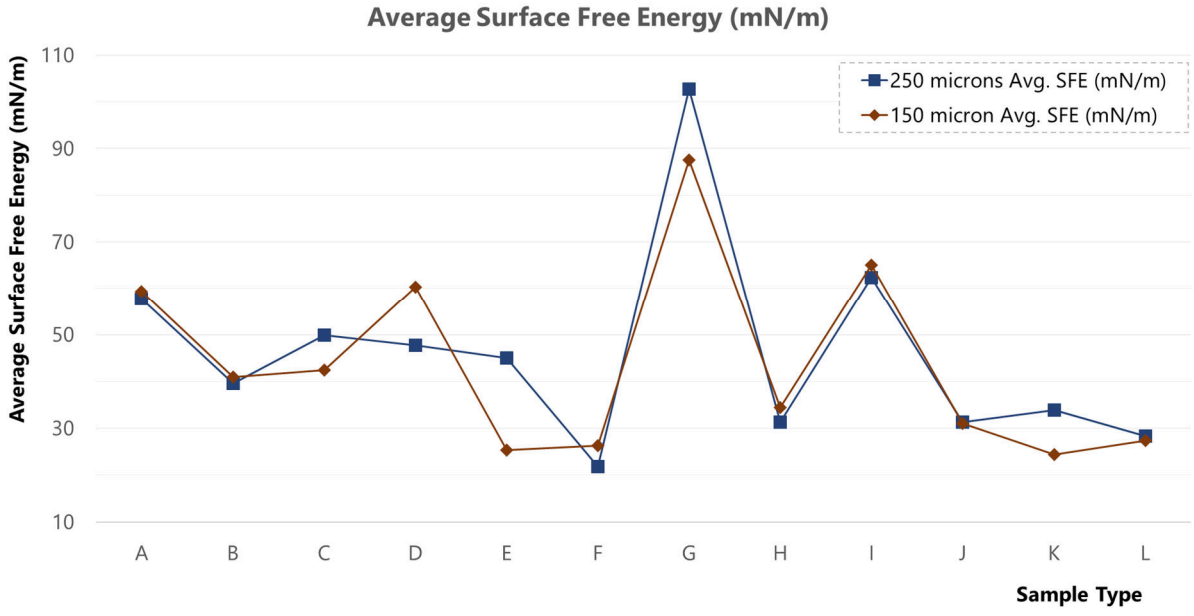

Figure 17: Average Surface Free Energy calculated using OWRK model for samples A - L prepared using 150- and 250-microns nozzles.

Overall, an increased SFE value indicates, increased wetting potential which results in low CAs with pinning of the target liquid while sliding. The average SFE calculated using this method compliments with our findings of surface wettability except for in sample F, where high adhesion of the Krytox GPL-105 repellent lubricant takes place on abraded MEK surface. This results in high CAs with water and glycerol but at the same time, limits the ability of the repellent liquid to flow freely in the micro- and nano- pores on the surface resulting in pinning of the contact line formed between repellent surface and target liquid, leading to high SAs.

Wear Failure Criterion

An important aspect to consider while reporting wear behaviour is to consider the failure criterion of our SLIPS. The failure modes that can occur during wear are shown in Figure 18 where in (b) and (c) the repellent liquid becomes trapped inside the structure which changes the wettability state. The wettability state now depends on the specific properties of the solid surface rather than on specific properties of the repellent lubricant. A combination of (b) and (c) states can also occur depending on the wear progress.

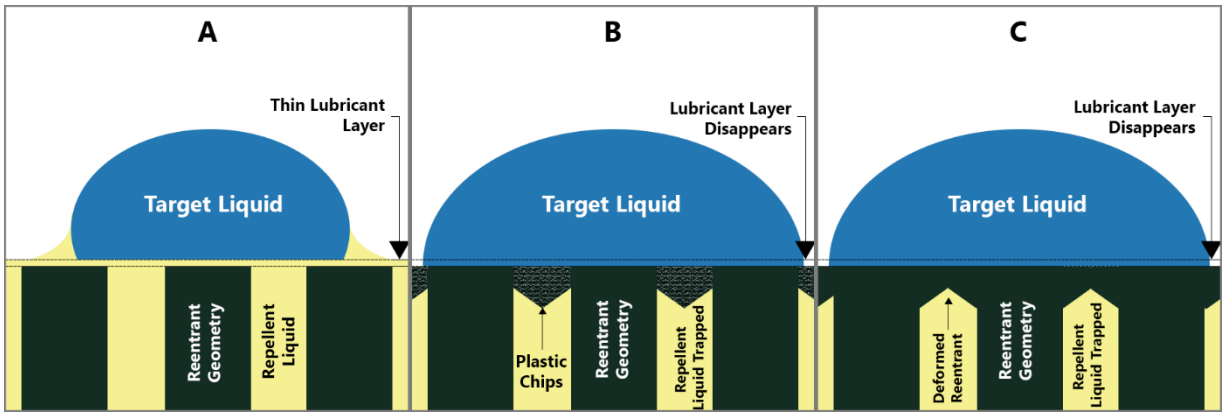

Figure 18: 2 important failure criterions for SLIPS geometry undergoing sliding wear. (a) shows the actual optimal SLIPS configuration where the target liquid rests over a thin lubricant layer of repellent liquid. In (b) the lubricant layer disappears due to chips (lose plastic) getting stuck in between the spacing in the reentrant geometry, while in (c), the top of the reentrant geometry deforms thereby blocking the space between reentrants.

The polymeric abrasive wear rate can be divided into 2 main types, which are cutting (Failure Mode B) and ploughing (Failure Mode C). The cutting wear as explained by Lancaster and Ratner [66] is proportional to the inverse of ultimate tensile stress and corresponding strain as given in Equation 5.

$$k_o \propto \frac{1}{\sigma_u \varepsilon_u} \tag{5}$$

where k_o is the wear coefficient measured in $mm^3(Nm)^{-1}$, σ_u is the ultimate tensile strength measured in $N(mm)^{-2}$ and ε_u is the corresponding strain.

On the other hand, the ploughing wear can be best described using the ploughing analogy presented by Myshkin et al [67]. This is when the ball pushes the printed line ahead of a particle which deforms the material sideways to form ridges across the developing groove.

These criterions are observed in our actual experiments as shown in Figure 19 where the wear track shows reentrant geometry diminishing over time. The coefficient of friction (μ) changes until a threshold value is reached after which it stabilizes which is common to all polymers [68]. However, the stabilization of coefficient of friction is achieved well after the failure criterion of our SLIPS geometry has occurred. This is an important result which shows that common wear

parameters such as track width and coefficient of friction cannot alone be used to identify the efficiency of SLIPS.

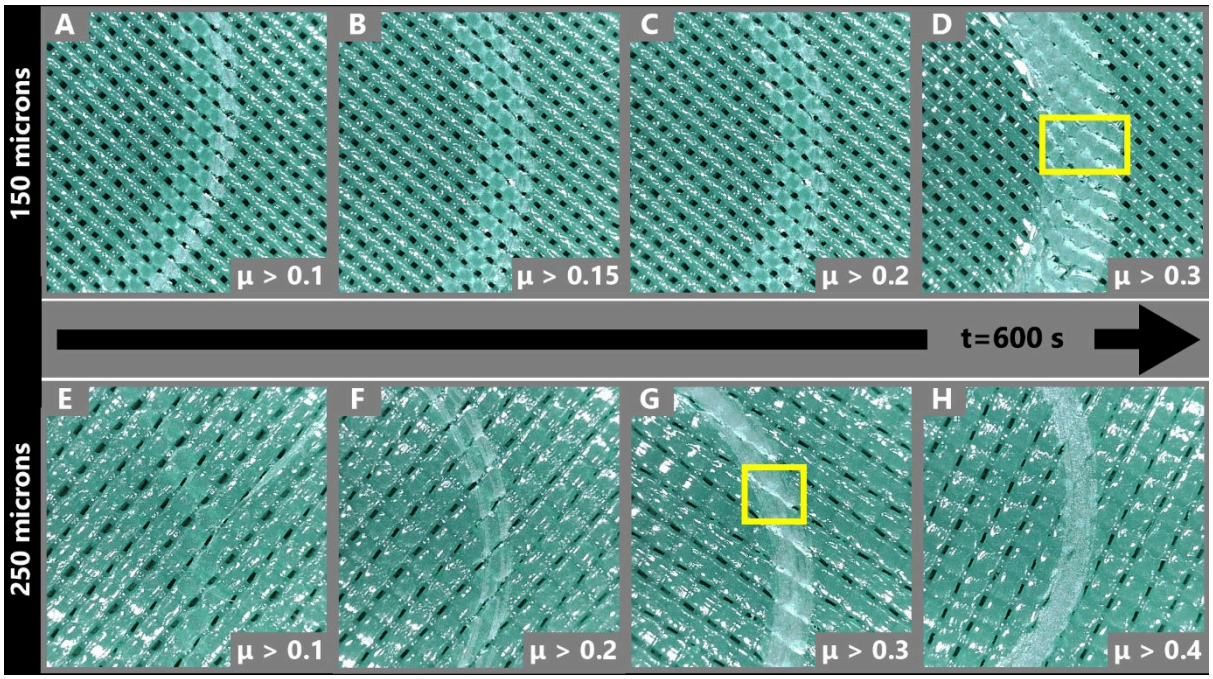

Figure 19: Progressive wear-track indicating an increase in track width and penetration depth as time progresses. As time progresses from 0 to 600s, the wear also progresses from (a – d) for 150 microns samples and (e – h) for 250 microns samples. An increase in μ shows more resistance to wear until μ reaches a threshold value after which it goes into constant sliding wear. The failure criterion occurs when the open to the reentrant geometry becomes blocked (yellow rectangle) due to lose eroded plastic settling in the grooves or deformation in adjacent lines due to sliding load.

However, it is pertinent to mention here that the occurrence of these failure criterion takes place at rigorous sliding loading conditions where 20 N load is applied continuously for 10 mins on the same sliding distance. Also, the change in COF is not equal for all samples which is attributed to differences in polymer deformation, where some samples continue to show low COF values over the investigated period. In these samples, only deformation of the reentrant geometry took place while the chips produced are sufficiently large which are unable to block the reentrant geometry completely. This allows for the reentrant geometry to function normally by continuously providing a thin layer of lubricating repellent liquid on top of reentrants allowing ease in rolling-off the target liquid.

Overall it can be stated, that if the reentrant geometry remains open with the repellent lubricant oil allowed to flow freely, the SLIPS will continue to demonstrate optimal surface wettability behaviour and good resistance to mechanical abrasion; based primarily on the strength of the 3D printed structure. Furthermore, since the surface on which the target liquid rests is not that of reentrants but a combination of reentrant and repellent liquid (interfacial surface), so a constant supply of the repellent liquid ensures that the surface remains self-healing in nature.

Conclusion

The work presented here is a continuation to the developments being undertaken in the study of fabrication of SLIPS by multiple authors. In identifying the knowledge gaps in the fabrication of scalable SLIPS, this work forms basis for the creation of a low-cost liquid retaining porous structure.

A two-step facile method based on Fused Deposition Modelling (FDM) is presented here for the design and manufacturing of the initial surface geometry with highly controllable micro-porosity capable of retaining the repellent liquid within it without any added treatment. The 3D micro-porous structure works by reducing the apparent contact area, providing space for lubricant storage (ensuring adequate replenishment source is available), giving the surface its intended strength, and combining layer-by-layer reentrant type geometrical features to develop robust SLIPS.

The micro- porosity is then enhanced to nano- porosity using chemical agents and amorphous fumed silica powder which enhances the efficiency of lubricant (repellent liquid) entrapment. After lubricant infusion, the surface demonstrates characteristic low SA with both polar and non-polar solvents and with high CA.

The SLIPS produced exhibit strong resistance to mechanical abrasion and exhibit good performance until their failure criterion occurs. The failure criterion models are based on the reentrant geometry sites (micro-pores) diminishing over time due to high sliding friction which results in lose plastic chips and structural deformation of nearby reentrants blocking the micro-pores.

The findings of this work can be summarized as follows.

1. The complex micro-porous geometry is obtained by using modifiers during the slicing process which removes limitation of intricate CAD modelling and therefore makes the porosity designing process scalable beyond laboratory use.
2. Due to the specific deposition process of the FDM machine, the surface initially formed shows anisotropic wettability which is then favourably transformed using chemical abrasion to exhibit isotropic wettability.
3. The chemical abrasion also created new liquid (oil) adsorption nano- sites for infusing the repellent liquid.
4. With the addition of hydrophobic fumed silica powder during the chemical abrasion process, the surface demonstrated complete isotropic wettability. Also, due to the hydrophobic nature of the fumed silica powder, the surface also demonstrated repellence against polar liquids. The fumed silica powder gives rise to increase in the oil adsorption sites where repellent oils (Silicone or Krytox (PTFE)) are easily infused resulting in extremely low sliding angles of up to 2° with both polar and non-polar liquids.
5. Alternatively, when the chemical abrasion was carried out without the addition of hydrophobic fumed silica, the surface is rendered extremely amphiphilic. The surface wettability is then categorically modified to exhibit amphiphobicity by the infusion of repellent oils (Silicone or Krytox (PTFE)).
6. Wear testing using harsh sliding loads was carried out on the 3D printed porous structures and low COF and Pd values were obtained which shows high resistance to mechanical abrasion.
7. The failure criterion of SLIPS occurred when the repellent lubricant oil is unable to form an interfacial layer on the top surface.

The route to the preparation of the porous structure for SLIPS using FDM 3D printing technique has been reported for the first time. Moreover, through this route it has been demonstrated that fabrication of scalable SLIPS is possible which has been a problematic area for researchers as evidenced in literature time and again [69,70]. This work therefore addresses

this important knowledge gap so that subsequent work towards scaling up of SLIPS can be carried out to allow for its eventual industrial use.

Acknowledgements

This work is jointly supported by Commonwealth Scholarship Commission in the UK (Grant No. PKCN-2019-405), Cranfield University, UK and National University of Sciences and Technology (NUST), Pakistan. The authors are grateful to Mr. Drew Murray of Cranfield Village, and Mr. Kristopher Bramley of Cranfield University for their support in this work.

List of References

[1] T.-S. Wong, S.H. Kang, S.K.Y. Tang, E.J. Smythe, B.D. Hatton, A. Grinthal, J. Aizenberg, Bioinspired self-repairing slippery surfaces with pressure-stable omniphobicity, Nature. 477 (2011) 443–447. https://doi.org/10.1038/nature10447.

[2] H.F. Bohn, W. Federle, Insect aquaplaning: Nepenthes pitcher plants capture prey with the peristome, a fully wettable water-lubricated anisotropic surface, Proc. Natl. Acad. Sci. U. S. A. 101 (2004) 14138–14143. https://doi.org/10.1073/pnas.0405885101.

[3] X. Lou, Y. Huang, X. Yang, H. Zhu, L. Heng, F. Xia, External Stimuli Responsive Liquid-Infused Surfaces Switching between Slippery and Nonslippery States: Fabrications and Applications, Adv. Funct. Mater. 30 (2020) 1901130. https://doi.org/10.1002/adfm.201901130.

[4] J. Yong, J. Huo, Q. Yang, F. Chen, Y. Fang, X. Wu, L. Liu, X. Lu, J. Zhang, X. Hou, Femtosecond Laser Direct Writing of Porous Network Microstructures for Fabricating Super-Slippery Surfaces with Excellent Liquid Repellence and Anti-Cell Proliferation, Adv. Mater. Interfaces. 5 (2018). https://doi.org/10.1002/admi.201701479.

[5] J.D. Smith, R. Dhiman, S. Anand, E. Reza-Garduno, R.E. Cohen, G.H. McKinley, K.K. Varanasi, Droplet mobility on lubricant-impregnated surfaces, Soft Matter. 9 (2013) 1772–1780. https://doi.org/10.1039/c2sm27032c.

[6] X. Yao, Y. Hu, A. Grinthal, T.S. Wong, L. Mahadevan, J. Aizenberg, Adaptive fluid-infused porous films with tunable transparency and wettability, Nat. Mater. 12 (2013) 529–534. https://doi.org/10.1038/nmat3598.

[7] Q. Wei, C. Schlaich, S. Prévost, A. Schulz, C. Böttcher, M. Gradzielski, Z. Qi, R. Haag, C.A. Schalley, Supramolecular polymers as surface coatings: Rapid fabrication of healable superhydrophobic and slippery surfaces, Adv. Mater. 26 (2014) 7358–7364. https://doi.org/10.1002/adma.201401366.

[8] J. Abe, M. Tenjimbayashi, S. Shiratori, Electrospun nanofiber SLIPS exhibiting high total transparency and scattering, RSC Adv. 6 (2016) 38018–38023. https://doi.org/10.1039/c6ra00276e.

[9] J.H. Guan, G.G. Wells, B. Xu, G. McHale, D. Wood, J. Martin, S. Stuart-Cole, Evaporation of Sessile Droplets on Slippery Liquid-Infused Porous Surfaces (SLIPS), Langmuir. 31 (2015) 11781–11789. https://doi.org/10.1021/acs.langmuir.5b03240.

[10] S. Anand, A.T. Paxson, R. Dhiman, J.D. Smith, K.K. Varanasi, Enhanced condensation on lubricant-impregnated nanotextured surfaces, ACS Nano. 6 (2012) 10122–10129. https://doi.org/10.1021/nn303867y.

[11] J. Chen, R. Dou, D. Cui, Q. Zhang, Y. Zhang, F. Xu, X. Zhou, J. Wang, Y. Song, L. Jiang, Robust prototypical anti-icing coatings with a self-lubricating liquid water layer between ice and substrate, ACS Appl. Mater. Interfaces. 5 (2013) 4026–4030. https://doi.org/10.1021/am401004t.

[12] S.B. Subramanyam, K. Rykaczewski, K.K. Varanasi, Ice adhesion on lubricant-impregnated

textured surfaces, Langmuir. 29 (2013) 13414–13418. https://doi.org/10.1021/la402456c.

[13] K.S. Khalil, S.R. Mahmoudi, N. Abu-Dheir, K.K. Varanasi, Active surfaces: Ferrofluid-impregnated surfaces for active manipulation of droplets, Appl. Phys. Lett. 105 (2014). https://doi.org/10.1063/1.4891439.

[14] P. Kim, T.S. Wong, J. Alvarenga, M.J. Kreder, W.E. Adorno-Martinez, J. Aizenberg, Liquid-infused nanostructured surfaces with extreme anti-ice and anti-frost performance, ACS Nano. 6 (2012) 6569–6577. https://doi.org/10.1021/nn302310q.

[15] R. Qiu, Q. Zhang, P. Wang, L. Jiang, J. Hou, W. Guo, H. Zhang, Fabrication of slippery liquid-infused porous surface based on carbon fiber with enhanced corrosion inhibition property, Colloids Surfaces A Physicochem. Eng. Asp. 453 (2014) 132–141. https://doi.org/10.1016/j.colsurfa.2014.04.035.

[16] P.W. Wilson, W. Lu, H. Xu, P. Kim, M.J. Kreder, J. Alvarenga, J. Aizenberg, Inhibition of ice nucleation by slippery liquid-infused porous surfaces (SLIPS), Phys. Chem. Chem. Phys. 15 (2013) 581–585. https://doi.org/10.1039/c2cp43586a.

[17] B.R. Solomon, K.S. Khalil, K.K. Varanasi, Drag reduction using lubricant-impregnated surfaces in viscous laminar flow, Langmuir. 30 (2014) 10970–10976. https://doi.org/10.1021/la5021143.

[18] N. Bjelobrk, H.L. Girard, S.B. Subramanyam, H.M. Kwon, D. Quéré, K.K. Varanasi, Thermocapillary motion on lubricant-impregnated surfaces, Phys. Rev. Fluids. 1 (2016). https://doi.org/10.1103/PhysRevFluids.1.063902.

[19] K. Rykaczewski, A.T. Paxson, M. Staymates, M.L. Walker, X. Sun, S. Anand, S. Srinivasan, G.H. McKinley, J. Chinn, J.H.J. Scott, K.K. Varanasi, Dropwise condensation of low surface tension fluids on omniphobic surfaces, Sci. Rep. 4 (2014) 1–8. https://doi.org/10.1038/srep04158.

[20] D.F. Miranda, C. Urata, B. Masheder, G.J. Dunderdale, M. Yagihashi, A. Hozumi, Physically and chemically stable ionic liquid-infused textured surfaces showing excellent dynamic omniphobicity, APL Mater. 2 (2014). https://doi.org/10.1063/1.4876636.

[21] S. Sunny, N. Vogel, C. Howell, T.L. Vu, J. Aizenberg, Lubricant-Infused Nanoparticulate Coatings Assembled by Layer-by-Layer Deposition, Adv. Funct. Mater. 24 (2014) 6658–6667. https://doi.org/10.1002/adfm.201401289.

[22] J. Guo, W. Fang, A. Welle, W. Feng, I. Filpponen, O.J. Rojas, P.A. Levkin, Superhydrophobic and Slippery Lubricant-Infused Flexible Transparent Nanocellulose Films by Photoinduced Thiol-Ene Functionalization, ACS Appl. Mater. Interfaces. 8 (2016) 34115–34122. https://doi.org/10.1021/acsami.6b11741.

[23] I. Okada, S. Shiratori, High-transparency, self-standable Gel-SLIPS fabricated by a facile nanoscale phase separation, ACS Appl. Mater. Interfaces. 6 (2014) 1502–1508. https://doi.org/10.1021/am404077h.

[24] N. Vogel, R.A. Belisle, B. Hatton, T.S. Wong, J. Aizenberg, Transparency and damage tolerance of patternable omniphobic lubricated surfaces based on inverse colloidal monolayers, Nat. Commun. 4 (2013). https://doi.org/10.1038/ncomms3176.

[25] N.R. Geraldi, J.H. Guan, L.E. Dodd, P. Maiello, B.B. Xu, D. Wood, M.I. Newton, G.G. Wells, G. McHale, Double-sided slippery liquid-infused porous materials using conformable mesh, Sci. Rep. 9 (2019) 13280. https://doi.org/10.1038/s41598-019-49887-3.

[26] P.B. Weisensee, Y. Wang, H. Qiang, D. Schultz, W.P. King, N. Miljkovic, Condensate droplet size distribution on lubricant-infused surfaces, Int. J. Heat Mass Transf. 109 (2017) 187–199. https://doi.org/10.1016/j.ijheatmasstransfer.2017.01.119.

[27] D. Seo, J. Shim, B. Moon, K. Lee, J. Lee, C. Lee, Y. Nam, Passive Anti-Flooding Superhydrophobic Surfaces, ACS Appl. Mater. Interfaces. 12 (2020) 4068–4080. https://doi.org/10.1021/acsami.9b17943.

[28] S. Sett, P. Sokalski, K. Boyina, L. Li, K.F. Rabbi, H. Auby, T. Foulkes, A. Mahvi, G. Barac, L.W. Bolton, N. Miljkovic, Stable Dropwise Condensation of Ethanol and Hexane on Rationally Designed Ultrascalable Nanostructured Lubricant-Infused Surfaces, Nano Lett. 19 (2019) 5287–5296. https://doi.org/10.1021/acs.nanolett.9b01754.

[29] J.Y. Ho, K.F. Rabbi, S. Sett, T.N. Wong, N. Miljkovic, Dropwise condensation of low surface tension fluids on lubricant-infused surfaces: Droplet size distribution and heat transfer, Int. J. Heat Mass Transf. 172 (2021) 16–20. https://doi.org/10.1016/j.ijheatmasstransfer.2021.121149.

[30] M. Nosonovsky, Slippery when wetted, Nature. 477 (2011) 412–413. https://doi.org/10.1038/477412a.

[31] L. Gao, Y. Liu, H. Hu, An experimental study on icing physics for wind turbine icing mitigation, 35th Wind Energy Symp. 2017. 162 (2017) 2344–2360. https://doi.org/10.1016/j.renene.2020.10.013.

[32] L. Xiao, J. Li, S. Mieszkin, A. Di Fino, A.S. Clare, M.E. Callow, J.A. Callow, M. Grunze, A. Rosenhahn, P.A. Levkin, Slippery liquid-infused porous surfaces showing marine antibiofouling properties, ACS Appl. Mater. Interfaces. 5 (2013) 10074–10080. https://doi.org/10.1021/am402635p.

[33] Y.H. Yeong, C. Wang, K.J. Wynne, M.C. Gupta, Oil-infused superhydrophobic silicone material for low ice adhesion with long-term infusion stability, ACS Appl. Mater. Interfaces. 8 (2016) 32050–32059. https://doi.org/10.1021/acsami.6b11184.

[34] P.B. Weisensee, Y. Wang, H. Qiang, D. Schultz, W.P. King, N. Miljkovic, Condensate droplet size distribution on lubricant-infused surfaces, Int. J. Heat Mass Transf. 109 (2017) 187–199. https://doi.org/10.1016/j.ijheatmasstransfer.2017.01.119.

[35] S. Zhou, C. Yu, C. Li, Z. Dong, L. Jiang, Programmable unidirectional liquid transport on peristome-mimetic surfaces under liquid environments, J. Mater. Chem. A. 7 (2019) 18244–18248. https://doi.org/10.1039/c9ta04770k.

[36] J. Ahn, Y. Jeon, K.W. Lee, J. Yi, S.W. Kim, D.R. Kim, D.R. Kim, Bactericidal Lubricating Synthetic Materials for Three-Dimensional Additive Assembly with Controlled Mechanical Properties, ACS Appl. Mater. Interfaces. 12 (2020) 26464–26475. https://doi.org/10.1021/acsami.0c05764.

[37] H. Shams, K. Basit, M.A. Khan, S. Saleem, A. Mansoor, Realizing surface amphiphobicity using 3D printing techniques: A critical move towards manufacturing low-cost reentrant geometries, Addit. Manuf. 38 (2021) 101777. https://doi.org/10.1016/j.addma.2020.101777.

[38] H. Shams, K. Basit, M.A. Khan, A. Mansoor, Wear Behavior of 3D Printed PLA Surfaces for Superhydrophobic Interaction, SSRN Electron. J. (2020). https://doi.org/10.2139/ssrn.3717991.

[39] D. Zhang, Y. Xia, X. Chen, S. Shi, L. Lei, PDMS-Infused Poly(High Internal Phase Emulsion) Templates for the Construction of Slippery Liquid-Infused Porous Surfaces with Self-cleaning and Self-repairing Properties, Langmuir. (2019). https://doi.org/10.1021/acs.langmuir.9b01115.

[40] X. Zhou, Y.Y. Lee, K.S.L. Chong, C. He, Superhydrophobic and slippery liquid-infused porous surfaces formed by the self-assembly of a hybrid ABC triblock copolymer and their antifouling performance, J. Mater. Chem. B. 6 (2018) 440–448. https://doi.org/10.1039/c7tb02457f.

[41] P. Agrawal, T.T. Salomons, D.S. Chiriac, A.C. Ross, R.D. Oleschuk, Facile Actuation of Organic and Aqueous Droplets on Slippery Liquid-Infused Porous Surfaces for the Application of On-Chip Polymer Synthesis and Liquid-Liquid Extraction, ACS Appl. Mater. Interfaces. 11 (2019) 28327–28335. https://doi.org/10.1021/acsami.9b08849.

[42] S. Habib, S. Zavahir, A.E. Abusrafa, A. Abdulkareem, P. Sobolčiak, M. Lehocky, D. Vesela, P. Humpolíček, A. Popelka, Slippery liquid-infused porous polymeric surfaces based on natural oil with antimicrobial effect, Polymers (Basel). 13 (2021) 1–18. https://doi.org/10.3390/polym13020206.

[43] Y. Liu, Y. Tian, J. Chen, H. Gu, J. Liu, R. Wang, B. Zhang, H. Zhang, Q. Zhang, Design and preparation of bioinspired slippery liquid-infused porous surfaces with anti-icing performance via delayed phase inversion process, Colloids Surfaces A Physicochem. Eng. Asp. 588 (2020) 124384. https://doi.org/10.1016/j.colsurfa.2019.124384.

[44] G.H. Zhu, S.H. Cho, H. Zhang, M. Zhao, N.S. Zacharia, Slippery Liquid-Infused Porous Surfaces (SLIPS) Using Layer-by-Layer Polyelectrolyte Assembly in Organic Solvent, Langmuir. 34 (2018) 4722–4731. https://doi.org/10.1021/acs.langmuir.8b00335.

[45] Q. Wu, C. Yang, C. Su, L. Zhong, L. Zhou, T. Hang, H. Lin, W. Chen, L. Li, X. Xie, Slippery Liquid-Attached Surface for Robust Biofouling Resistance, ACS Biomater. Sci. Eng. 6 (2020) 358–366. https://doi.org/10.1021/acsbiomaterials.9b01323.

[46] R. Mukherjee, M. Habibi, Z.T. Rashed, O. Berbert, X. Shi, J.B. Boreyko, Oil-Impregnated Hydrocarbon-Based Polymer Films, Sci. Rep. 8 (2018) 1–13. https://doi.org/10.1038/s41598-018-29823-7.

[47] A. Nakajima, A. Fujishima, K. Hashimoto, T. Watanabe, Preparation of Transparent Superhydrophobic Boehmite and Silica Films by Sublimation of Aluminum Acetylacetonate, Adv. Mater. 11 (1999) 1365–1368. https://doi.org/10.1002/(SICI)1521-4095(199911)11:16<1365::AID-ADMA1365>3.0.CO;2-F.

[48] K. Tadanaga, J. Morinaga, A. Matsuda, T. Minami, Superhydrophobic - Superhydrophilic micropatterning on flowerlike alumina coating film by the sol - Gel method, Chem. Mater. 12 (2000) 590–592. https://doi.org/10.1021/cm990643h.

[49] X.B. Wang, Y.Q. Liu, D.B. Zhu, Honeycomb-like alignments of carbon nanotubes synthesized by pyrolysis of a metal phthalocyanine, Appl. Phys. A Mater. Sci. Process. 71 (2000) 347–348. https://doi.org/10.1007/s003390000604.

[50] L. Jiang, R. Wang, B. Yang, T.J. Li, D.A. Tryk, A. Fujishima, K. Hashimoto, D.B. Zhu, Binary cooperative complementary nanoscale interfacial materials, Pure Appl. Chem. 72 (2000) 73–81. https://doi.org/10.1351/pac200072010073.

[51] D. Öner, T.J. McCarthy, Ultrahydrophobic surfaces. Effects of topography length scales on wettability, Langmuir. 16 (2000) 7777–7782. https://doi.org/10.1021/la000598o.

[52] C.W. Extrand, Criteria for ultralyophobic surfaces, Langmuir. 20 (2004) 5013–5018. https://doi.org/10.1021/la036481s.

[53] M. Nosonovsky, B. Bhushan, Why re-entrant surface topography is needed for robust oleophobicity, Philos. Trans. R. Soc. A Math. Phys. Eng. Sci. 374 (2016). https://doi.org/10.1098/rsta.2016.0185.

[54] J.H. Shin, J. Heo, S. Jeon, J.H. Park, S. Kim, Bio-inspired hollow PDMS sponge for enhanced oil – water separation, J. Hazard. Mater. 365 (2019) 494–501. https://doi.org/10.1016/j.jhazmat.2018.10.078.

[55] A. Li, H.-X. Sun, D.-Z. Tan, W.-J. Fan, S.-H. Wen, X.-J. Qing, G.-X. Li, S.-Y. Li, W.-Q. Deng, Superhydrophobic conjugated microporous polymers for separation and adsorption, Energy Environ. Sci. 4 (2011) 2062. https://doi.org/10.1039/c1ee01092a.

[56] G. Jiang, R. Hu, X. Xi, X. Wang, R. Wang, Facile preparation of superhydrophobic and superoleophilic sponge for fast removal of oils from water surface, J. Mater. Res. 28 (2013) 651–656. https://doi.org/10.1557/jmr.2012.410.

[57] J. Sun, P.B. Weisensee, Microdroplet self-propulsion during dropwise condensation on lubricant-infused surfaces, Soft Matter. 15 (2019) 4808–4817. https://doi.org/10.1039/c9sm00493a.

[58] X. He, P. Cao, F. Tian, X. Bai, C. Yuan, Infused configurations induced by structures influence stability and antifouling performance of biomimetic lubricant-infused surfaces, Surf. Coatings

Technol. 358 (2019) 159–166. https://doi.org/10.1016/j.surfcoat.2018.11.035.

[59] J.H. Kim, M.J. Kim, B. Lee, J.M. Chun, V. Patil, Y.S. Kim, Durable ice-lubricating surfaces based on polydimethylsiloxane embedded silicone oil infused silica aerogel, Appl. Surf. Sci. 512 (2020) 145728. https://doi.org/10.1016/j.apsusc.2020.145728.

[60] P. Zhang, H. Chen, L. Zhang, Y. Zhang, D. Zhang, L. Jiang, Stable slippery liquid-infused anti-wetting surface at high temperatures, J. Mater. Chem. A. 4 (2016) 12212–12220. https://doi.org/10.1039/c6ta03857c.

[61] Y. Cao, S. Jana, X. Tan, L. Bowen, Y. Zhu, J. Dawson, R. Han, J. Exton, H. Liu, G. McHale, N.S. Jakubovics, J. Chen, Antiwetting and Antifouling Performances of Different Lubricant-Infused Slippery Surfaces, Langmuir. 36 (2020) 13396–13407. https://doi.org/10.1021/acs.langmuir.0c00411.

[62] G. McHale, B. V. Orme, G.G. Wells, R. Ledesma-Aguilar, Apparent Contact Angles on Lubricant-Impregnated Surfaces/SLIPS: From Superhydrophobicity to Electrowetting, Langmuir. 35 (2019) 4197–4204. https://doi.org/10.1021/acs.langmuir.8b04136.

[63] C. Semprebon, G. McHale, H. Kusumaatmaja, Apparent contact angle and contact angle hysteresis on liquid infused surfaces, Soft Matter. 13 (2017) 101–110. https://doi.org/10.1039/C6SM00920D.

[64] M.J. Kreder, D. Daniel, A. Tetreault, Z. Cao, B. Lemaire, J.V.I. Timonen, J. Aizenberg, Film Dynamics and Lubricant Depletion by Droplets Moving on Lubricated Surfaces, Phys. Rev. X. 8 (2018) 031053. https://doi.org/10.1103/PhysRevX.8.031053.

[65] D.K. Owens, R.C. Wendt, Estimation of the surface free energy of polymers, J. Appl. Polym. Sci. 13 (1969) 1741–1747. https://doi.org/10.1002/app.1969.070130815.

[66] J.K. Lancaster, Relationships between the Wear of Polymers and their Mechanical Properties, Proc. Inst. Mech. Eng. Conf. Proc. 183 (1968) 98–106. https://doi.org/10.1243/PIME_CONF_1968_183_283_02.

[67] N.K. Myshkin, D. V. Tkachuk, Polymer Tribology Fundamentals, in: Encycl. Tribol., Springer US, Boston, MA, 2013: pp. 2614–2619. https://doi.org/10.1007/978-0-387-92897-5_817.

[68] Nanovea, Tribology of Polymers using the Nanovea T2000, 2019. https://nanovea.com/App-Notes/tribology-of-polymers.pdf.

[69] R. Deng, T. Shen, H. Chen, J. Lu, H.C. Yang, W. Li, Slippery liquid-infused porous surfaces (SLIPSs): A perfect solution to both marine fouling and corrosion?, J. Mater. Chem. A. 8 (2020) 7536–7547. https://doi.org/10.1039/d0ta02000a.

[70] C. Huang, Z. Guo, Fabrications and Applications of Slippery Liquid-infused Porous Surfaces Inspired from Nature: A Review, J. Bionic Eng. 16 (2019) 769–793. https://doi.org/10.1007/s42235-019-0096-2.

Supplementary Information
Scalable Wear Resistant 3D Printed Slippery Liquid Infused Porous Surfaces (SLIPS)

Hamza Shams[1,2], Kanza Basit[2], Muhammad Ali Khan[1], Asif Mansoor[2], Sajid Saleem[2]
[1]*Cranfield University, United Kingdom*
[2]*National University of Sciences and Technology (NUST), Pakistan*

Refer to Section, Design of SLIPS

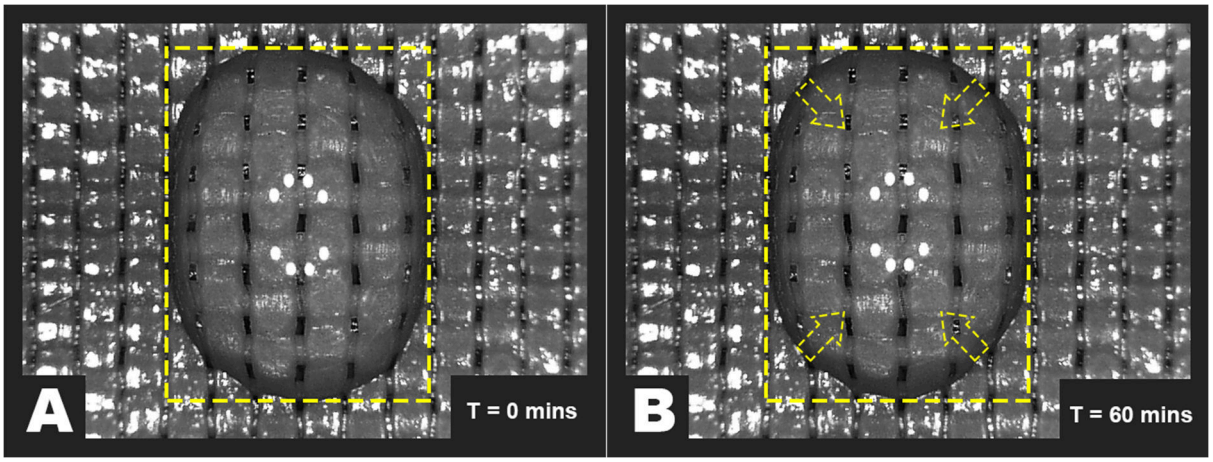

Figure 1: A) 20µl double distilled water droplet (target liquid 1) resting on the top surface at T=0 mins while, B) shows the same droplet after T=60 mins with slight evaporation losses resulting in droplet shrinkage from the sides. No air bubbles are observed during this entire time as can be seen from the images.

Refer to Section, Experimental Methodology

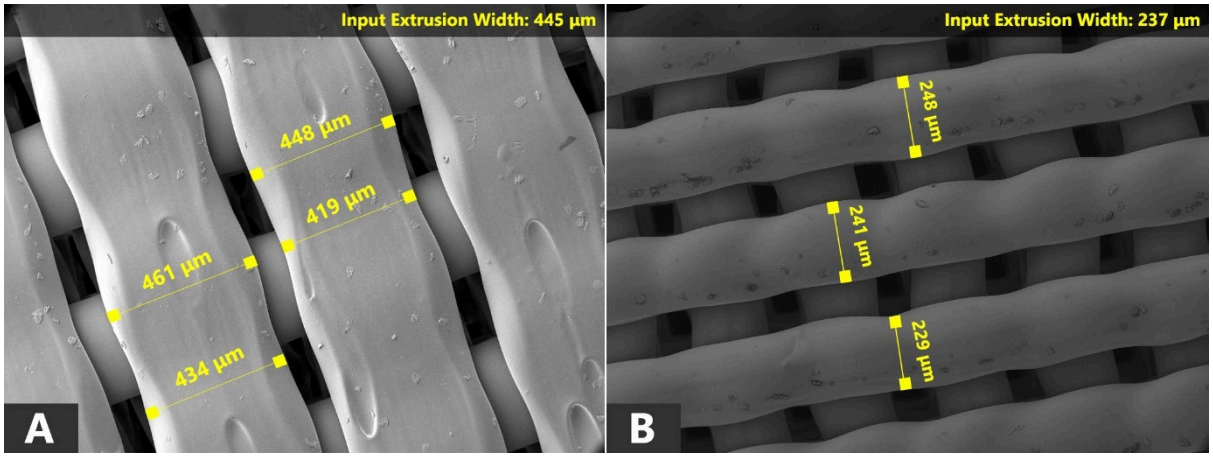

Figure 2: Comparison of input parameter (extrusion width) with as-built part. A) Shows the top-view of the sponge pattern fabricated using 250- µm nozzle while B) shows the top-view of the sponge pattern fabricated using 150- µm nozzle. In both cases, the averaged error between the input parameter (extrusion width) and actual dimension remains near to 3%.

Refer to Section, Experimental Methodology

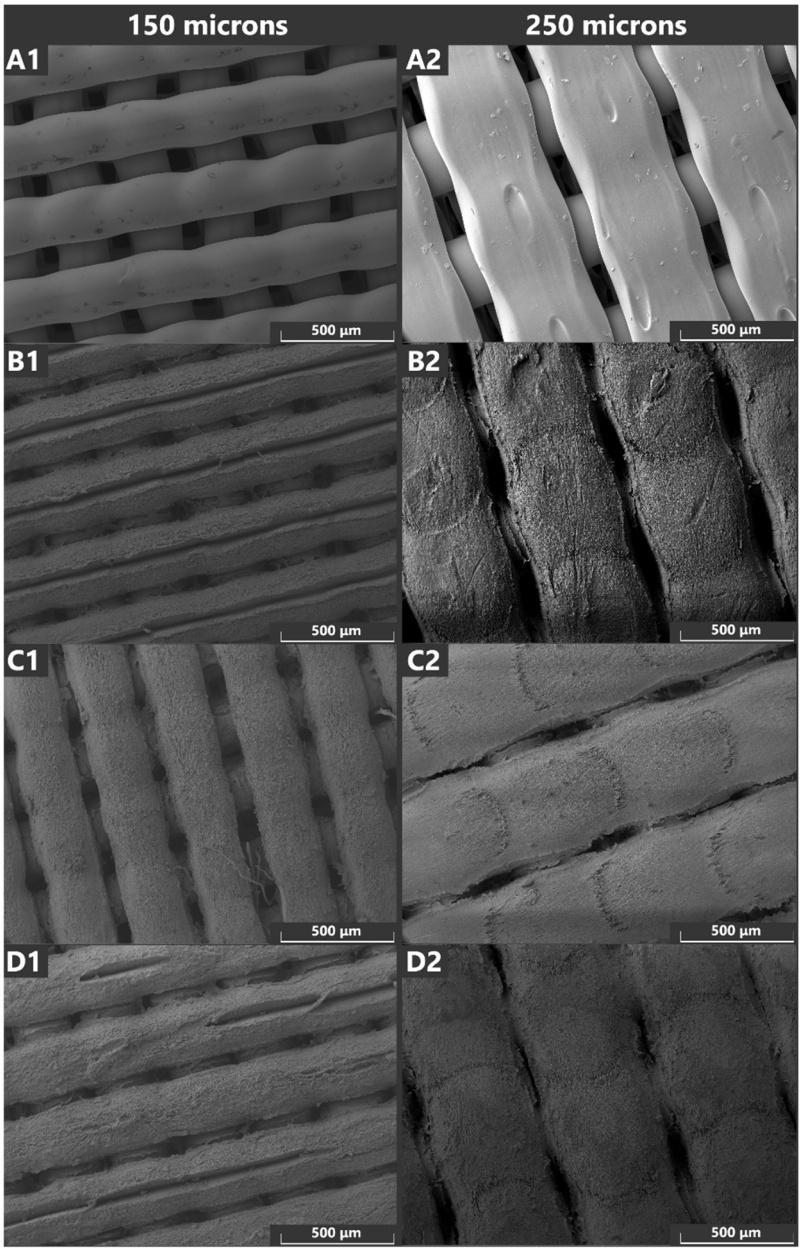

Figure 3: Scanning electron micrographs at 160x magnification of control samples prepared using 150- and 250- µm nozzles before entrapment of liquid. The 1 and 2 suffix denote 150- and 250- µm respectively. The (a) shows Sample A (b) shows Sample D, (c) shows Sample G and (d) shows Sample J after undergoing control treatments.

Refer to Section, Results

Note: For Tables 1 – 4, the average static contact angle in a specific direction is recorded over 3 to 5 readings. The standard deviation (SD) value represents the variation between these values which also provides an estimation of error in recording of each value.

Table 1: Average static contact angles (CA) with water in AC and BD direction for specimens 3D printed using 250 microns nozzle

Average static CA with water including SD for 250 microns samples				
S/No.	AC Direction		BD Direction	
	Average Static CA	SD	Average Static CA	SD
1	87.7	1.572	58.0	0.764
2	89.6	0.907	78.3	0.520
3	80.0	1.888	72.1	0.306
4	78.1	0.361	75.4	0.757
5	91.1	1.345	86.9	0.656
6	80.0	1.000	85.8	0.656
7	81.9	3.037	72.4	1.767
8	97.3	0.153	95.0	0.153
9	92.0	1.102	87.0	1.102
10	99.7	0.557	98.4	0.173
11	94.5	0.586	91.5	0.586
12	115.0	0.800	117.0	0.361

Table 2: Average static contact angles (CA) with glycerol in AC and BD direction for specimens 3D printed using 250 microns nozzle

Average static CA with glycerol including SD for 250 microns samples				
S/No.	AC Direction		BD Direction	
	Average Static CA	SD	Average Static CA	SD
1	72.6	0.985	51.7	0.755
2	80.2	0.500	74.5	1.650
3	75.0	1.320	62.0	0.200
4	80.0	0.321	60.9	0.896
5	76.2	0.693	69.9	1.845
6	96.0	0.451	92.0	3.592
7	20.5	0.723	17.1	0.153
8	88.3	0.252	82.6	3.166
9	60.0	0.751	58.0	2.303
10	96.4	0.400	75.9	3.156
11	83.9	1.850	81.8	0.289
12	90.0	2.751	86.0	2.318

Table 3: Average static contact angles (CA) with water in AC and BD direction for specimens 3D printed using 150 microns nozzle

Average static CA with water including SD for 150 microns samples				
S/No.	AC Direction		BD Direction	
	Average Static CA	SD	Average Static CA	SD
1	85.0	1.136	50.0	2.219
2	101.0	2.479	96.0	1.002
3	88.0	1.935	81.0	3.361
4	105.0	0.404	76.0	0.603
5	102.0	2.762	100.0	2.066
6	97.0	0.802	96.0	2.458
7	91.0	2.433	65.0	2.458
8	95.0	2.627	96.0	1.405
9	96.0	2.627	85.0	1.179
10	92.0	0.850	85.0	1.528
11	110.0	0.503	108.0	0.529
12	110.0	0.889	115.0	1.750

Table 4: Average static contact angles (CA) with glycerol in AC and BD direction for specimens 3D printed using 150 microns nozzle

Average static CA with glycerol including SD for 150 microns samples				
S/No.	AC Direction		BD Direction	
	Average Static CA	SD	Average Static CA	SD
1	68.0	1.015	53.0	1.908
2	83.0	0.985	71.0	3.361
3	79.0	2.515	71.0	3.700
4	65.0	2.203	55.0	2.458
5	91.0	0.814	92.0	0.850
6	92.5	2.237	88.0	2.558
7	88.0	0.252	46.0	1.405
8	82.0	1.779	83.0	0.985
9	55.0	0.961	58.0	0.252
10	93.0	2.739	78.0	0.300
11	94.0	2.739	92.0	0.850
12	92.0	0.850	87.0	1.102

Refer to Section, Further Discussion

Table 5: Polar and Dispersive components of Distilled Water and Glycerol [1]

Liquid	γ	γ_d	γ_p
Distilled Water	72.8	21.8	51
Glycerol	63.4	37	26.4

References

[1] R. C. R., S.P. Sundaran, J. A., S. Athiyanathil, Fabrication of superhydrophobic polycaprolactone/beeswax electrospun membranes for high-efficiency oil/water separation, RSC Adv. 7 (2017) 2092–2102. https://doi.org/10.1039/C6RA26123J.

https://dspace.org/

Scalable wear resistant 3D printed slippery liquid infused porous surfaces (SLIPS)

Shams, Hamza; Basit, Kanza; Khan, Muhammad Ali; Mansoor, Asif; Saleem, Sajid

2021-10-02
Elsevier
https://doi.org/10.1016/j.addma.2021.102379
Shams H, Basit K, Khan MA, et al., (2021) Scalable wear resistant 3D printed slippery liquid infused porous surfaces (SLIPS). Additive Manufacturing, Volume 48, Part A, December 2021, Article number 102379

Downloaded from a DSpace repository. https://dspace.org/